

A data analysis pipeline for the 26 m Hartebeesthoek radio telescope

Masterarbeit

vorgelegt von
Thorsten Brand

Erlangen Centre for Astroparticle Physics
Physikalisches Institut
Friedrich-Alexander-Universität
Erlangen-Nürnberg

1. Gutachter: Prof. Dr. Jörn Wilms
2. Gutachter: Prof. Dr. Matthias Kadler

Tag der Abgabe: 18.12.2013



Contents

1. The 26 m Hartebeesthoek radio telescope	6
1.1. A short history of radio telescopes	6
1.2. The components and physics of a radio telescope	8
1.2.1. Technical composition	8
1.2.2. Mount types and coordinate systems	9
1.2.3. Coordinate transformations	9
1.2.4. Optical properties	13
1.2.5. Receiver systems and signal processing	16
1.3. The 26 m Hartebeesthoek radio telescope in detail	17
2. The analysis of radio data	20
2.1. Scanning strategies and coordinate systems	20
2.2. The input data format	21
2.3. General analysis pipeline layout	22
2.4. The calibration database	22
2.5. The fit	24
2.6. Uncertainty estimation	28
2.7. Measurement of the PSF	29
2.8. The analysis database	30
2.9. Calibration sources and the calibration source database	30
2.10. Flux density calibration	32
3. Analyzing 8 years of PKS 0637-752-data	33
3.1. The data	33
3.2. Beam fitting	33
3.3. Calibration source data	39
3.4. The lightcurve of PKS 0637-752	46
4. Conclusions and Outlook	52
5. Abbreviations	53
A. Appendix	54
A.1. CIF binary table definition	54
A.2. CIF utility tools	55
A.2.1. Ingesting calibration files	55
A.2.2. Removing calibration files	56
A.3. Beam fitting program	56
A.4. Fit output file definition	58
A.5. ADB binary table definition	59
A.6. Filtering ADB files	61
A.7. CSDB binary table definition	62
A.8. Ingesting calibration source observations	63
A.9. Calibrating source flux densities	64
A.10. Flux calibration output definition	65

The Hartebeesthoek 26 m radio telescope provides a huge sample of single dish observations of various Active Galactic Nuclei (AGN) which have not been analyzed in detail yet. In this work, an automated data analysis pipeline for this telescope is presented. It fits a model consisting of the beam pattern as two-dimensional function and individual linear functions for the background of each subscan to the data sets and thus extracts the amplitude of the sources' signals. The model is extendable to correct for gravitational deformations of the beam pattern. By comparison with calibration source observations, the flux density of unknown objects can be obtained. The software is tested and the fitting quality is examined. First results are shown on the basis of an exemplary lightcurve analysis of the source PKS 0637-752. By using different calibrators, difficulties in the calibration process are described. An oscillation with the period of one year has been found in the calibration factor time evolution. By comparison with the respective curves, a correlation of this feature with the angular distance of the observed source and the Sun is found.

1. The 26 m Hartebeesthoek radio telescope

1.1. A short history of radio telescopes

When somebody is asked today how he pictures astronomers, he will most probably answer “looking through a spy-glass at night and watching the stars”. While this surely has been true in a certain way for astronomers since light collecting devices had been directed towards the night’s sky for the first time, the work routine became much more versatile during the last century.

With the discovery of visible light being just a small part of the electromagnetic spectrum and the invention of detectors to investigate other parts of it, physicists got the tools to examine processes of energy ranges and distances mankind could not even have dreamed of before.

One of these new instruments is the radio telescope. It aims at the low energetic end of the electromagnetic spectrum, below the infrared. The first of its kind which brought new insight in the field of astronomy was used by Karl Jansky after 1931, who discovered that radio emission is coming from the universe (Rohlf & Wilson, 2000, p. 1).

While Jansky’s telescope was an array of 20.5 MHz-dipole antennas (see Fig. 1.1) without a focusing optic (Verschuur et al., 1988, p. 1), Grote Reber built the first steerable radio telescope with a parabolic reflector (Verschuur, 2007, p. 14), in principle the type of instrument which is used today.

The Second World War accelerated the development of radio detection methods for radar technology. After the war, this technology and know-how could also be used in astronomy. This was also the time when radio astronomers first realized that the low spatial resolution of radio telescopes can be overcome by using the same methods that Michelson invented for optical interference observations to determine the angular diameter of stars (Verschuur, 2007; Ryle & Vonberg, 1948; Stanier, 1950).

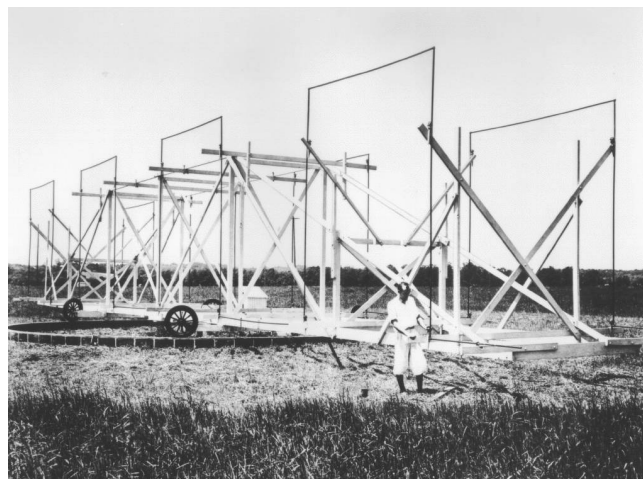


Figure 1.1.: Jansky’s radio dipole array (Source: <http://www.nrao.edu/whatisra/images/jansky1.gif>).

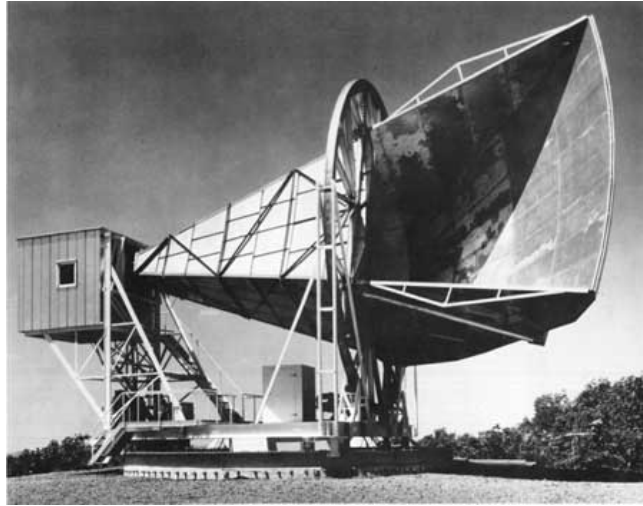


Figure 1.2.: The Holmdel Horn Antenna (Source: http://www.nps.gov/history/history/online_books/butowsky5/astro4k.htm).

Soon afterwards, the technology of ten years ago would not have been sufficient for the new scientific field, so large antennas were built specifically for astronomical purposes.

While most of them followed the scheme of Reber's parabolic mirror antenna, there were also new types. One of them is the Holmdel Horn Antenna (see Fig. 1.2). This telescope had also a mirror, but instead of the central section, it uses an area located more outwards of the paraboloid to reflect the radio waves perpendicularly into a horn-like tube. On the other end, the receiver is placed to measure the radiation (Crawford et al., 1961). With this instrument, the Cosmic Microwave Background was discovered by Penzias & Wilson (1965).

At the beginning of the 1960's, the famous radio telescope near Arecibo in Puerto Rico was built (Gordon & Lalonde, 1961). Its 1000-foot- or about 300 m-diameter dish is constructed in a natural valley and thus not steerable. However, by moving the secondary mirror and the following equipment which floats above the dish, supported by cables, the telescope can observe sources 20° around the zenith.

In the early 1970's, the Effelsberg 100 m telescope was finished to be the world's largest steerable telescope at the time. The size of the reflector required a new kind of structure to counteract deformations of the dish under its own weight. Therefore, the principle of "homologous deformation" was used. This new approach substituted the rigid support structure with a special, elastic structure which allowed deformations which result in a new paraboloid surface. This makes the focus shift depending on the pointing direction but ensures a surface accuracy good enough to focus radiation down to wavelengths of only a few millimeters (Hachenberg et al., 1973).

There is one radio telescope that is even larger than the Arecibo dish: The RATAN-600 telescope near Zelenchukskaya in the former Soviet Union has a diameter of 576 m. This instrument has no continuous primary mirror dish but consists of panels which form a ring, focusing the radiation to secondary mirrors in the center. The total collecting area of this telescope is smaller than the Arecibo telescope's by a factor of 6 (Korolkov & Pariiskii, 1979).

With this telescope it seems that the limit of single-dish telescopes is reached. In modern radio astronomy, interferometry is used for spatially resolved observations. With new methods for adding the signals and processing them further, the effectivity of this technique could be improved drastically (Kellermann & Moran, 2001).

The Very Large Array (VLA), an interferometrical combination of 27 antennas of 25 m diameter each in New Mexico, went into service in the late 1970's for astronomical research (Thompson

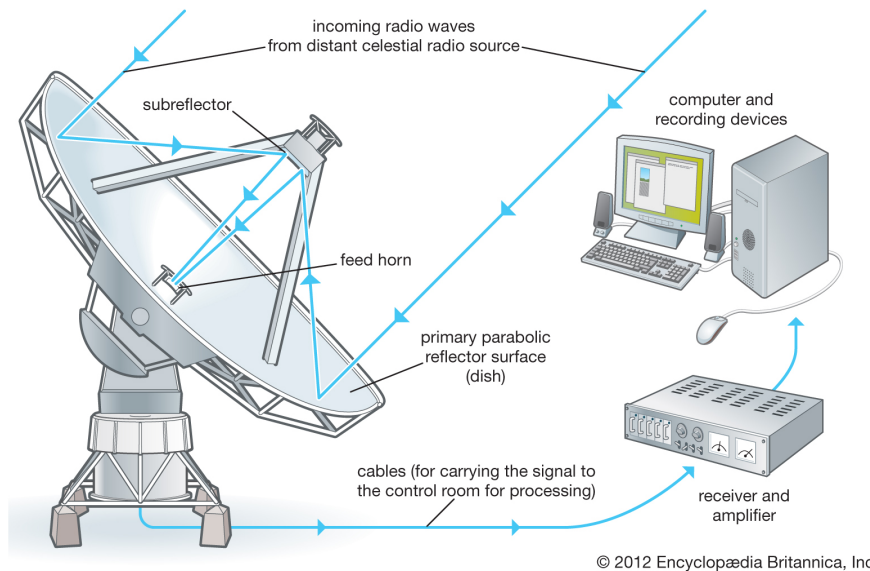


Figure 1.3.: A scheme of a typical radio telescope (Source: <http://media.web.britannica.com/eb-media/34/4634-050-DA53D88D.jpg>).

et al., 1980). The telescopes' signals are combined in a process called “aperture synthesis”. This method aims at artificially constructing a telescope with a spatial resolution equivalent to a dish with the diameter of the distances between the individual mirrors. With this approach, the VLA can resolve structures with sizes smaller than arc seconds. Between 2001 and 2012, the array has been refurbished, improving its sensitivity and frequency coverage drastically (Perley et al., 2011). Since 2012, it is renamed as the Karl G. Jansky Very Large Array.

The same method as on the VLA can be used to connect telescopes on different continents on earth, and even earthbound instruments with dishes on satellites like RadioAstron (Kardashev et al., 2012). With this satellite, baselines up to 350,000 km can be built. At a wavelength of 1.3 cm this equals a resolution of $7 \mu\text{s}$.

1.2. The components and physics of a radio telescope

1.2.1. Technical composition

A common radio telescope can be separated into three main components:

1. Mount
2. Optics
3. Receiver

The mount holds the large reflector dish and points it towards the desired direction. The radiation is collected and focused by a mirror system. At the focal point, it is caught by the feed and measured by the receiver. In Fig. 1.3 a scheme of the components can be seen.

In the following sections, the function and properties of these components will be described in more detail.

1.2.2. Mount types and coordinate systems

Astronomical telescopes need to be stabilized in every wavelength regime for making precise measurements of faint sources possible. But with Earth rotating relatively against the celestial objects, the mount also needs to enable the tracking of fixed points on the sky.

The most elegant way to achieve this is the equatorial mount. This type of mount is characterized by having two axes which allow rotations around the natural celestial coordinate axes for observations from Earth, Right Ascension (ra) and Declination (dec). Here ra is the axis parallel to the rotation of the Earth, and dec marks the height above the equator (see Fig. 1.4a).

Most modern optical and radio telescopes are using the alt-azimuthal mount. This mount type is the standard for Earth-bound observations and the most obvious way to mount a device, allowing to point it at every angle on the sphere. Its one coordinate axis, following the force of gravity in vertical direction, is called Azimuth (az) axis. It enables rotating the telescope like the needle of a compass. Variation of the angle on the second axis, the Altitude or Elevation (el) axis, sets the altitude of the pointing (see Fig. 1.4b).

While the alt-azimuthal mount is simpler and easier to construct, it has two disadvantages compared to the equatorial mount. First it is unable to track a celestial object over a period of time by only rotating around one axis. Second, when an astronomical object is tracked on an alt-azimuthal mount by rotating around two axes, the image of a non-point like source will smear over time by the rotation of the image field. This feature is very important when using imaging detectors and must then be corrected by a third axis which slowly compensates this rotation by counter-rotating the camera.

1.2.3. Coordinate transformations

The alt-azimuthal and equatorial systems are two spherical coordinate systems with very complicated dependencies. While the alt-azimuthal system is bound to a certain place on Earth's surface with a longitude λ and a latitude ϕ , it will follow all movements of this celestial

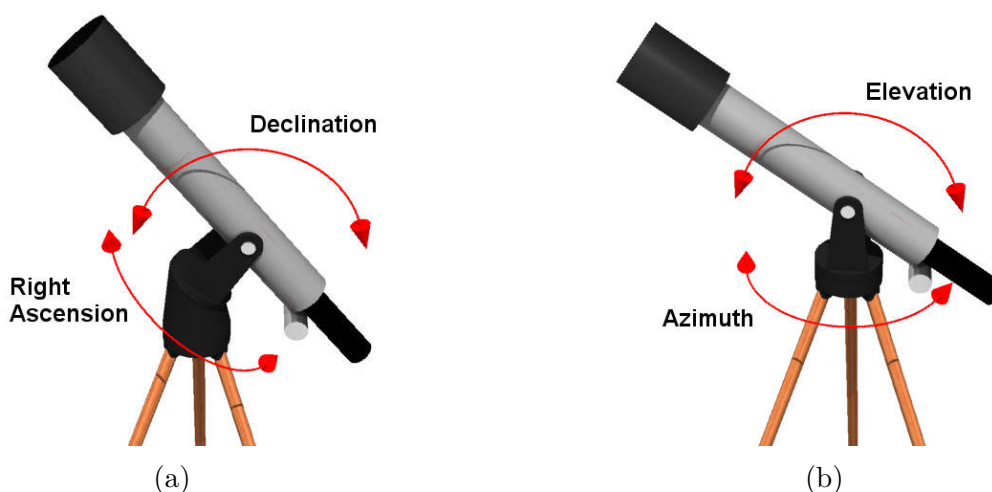


Figure 1.4.: Two mount types. A practical way for astronomical instruments is to mount them with the axes parallel to the equatorial coordinate axes (a). This “equatorial mount” has the advantage of tracking objects while earth rotates by rotating only around one axis. The “alt-azimuthal mount” (b) is easier to construct and follows the natural coordinate system for observations on earth.

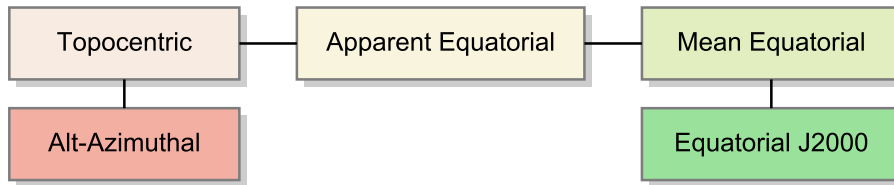


Figure 1.5.: A scheme of the coordinate transformation steps from alt-azimuthal coordinates to equatorial coordinates of the standard epoch J2000.

body. To convert the coordinates between the two systems, it is necessary to take these movements into account.

The basic scheme of the conversion process used for the analysis as described in this work is illustrated in Fig. 1.5. It is convenient to do the calculation in four steps, starting with either alt-azimuthal or equatorial coordinates.

In the following, the way from alt-azimuthal to standard equatorial coordinates of a certain epoch is described. The calculations are mostly excerpted from Seidelmann et al. (1992). As the aim is not to make high-precision coordinate measurements, not all effects of this complex topic are implemented and discussed here.

Rectangular coordinates

The coordinate transforms described in the following convert between spherical coordinate systems. Such transformations are accomplished by rotations. For calculation efficiency, they are done in rectangular coordinates by using rotation matrices.

The rectangular coordinates \mathbf{r} of a spherical coordinate system with azimuth α and elevation β are defined as

$$\mathbf{r} = \begin{pmatrix} x \\ y \\ z \end{pmatrix} = \begin{pmatrix} \cos \beta \cos \alpha \\ \cos \beta \sin \alpha \\ \sin \beta \end{pmatrix}. \quad (1.1)$$

Here, in the case of equatorial coordinates, α is replaced by ra and β by dec . In alt-azimuthal coordinates, az takes the place of α and el of β .

Topocentric coordinates

The starting point for the calculation are the alt-azimuthal coordinates az and el which describe the direction of a point in relation to the horizon. The first step is to transform them into a system which is aligned with the rotation of the Earth but which is still based on the same location on the surface. This is the topocentric system with the coordinates H and dec , where H is called the hour angle, and describes the angle between the object and the meridian. It is connected to ra with the Local Mean Sidereal Time (LMST) in the formula given by Meeus (1998, p. 92):

$$ra = H + \text{LMST} \quad (1.2)$$

To convert alt-azimuthal to topocentric coordinates, the rectangular vector of the alt-azimuthal system has to be rotated around the y -axis by an angle of $\phi - 90^\circ$, which is the distance between the celestial pole and the zenith. Because of different definitions of the azimuth to be measured not from the South but from the North, another rotation around the new z -axis by 180° may be necessary.

Apparent equatorial coordinates

With Eq. 1.2, the hour angle can be converted to the right ascension by knowing the LMST.

To get the LMST, the Greenwich Mean Sidereal Time (GMST) can be calculated before from a given longitude corrected Universal Time (UT1) value using the formula

$$\text{GMST1} = 24110^s.54841 + 8640184^s.812866 T_u + 0^s.093104 T_u^2 - 0^s.0000062 T_u^3 \quad (1.3)$$

with $T_u = d_u/36525$ and d_u being the number of days elapsed since JD 2451545.0 UT1. Adding the astronomical longitude λ of the observer gives the LMST:

$$\text{LMST} = \text{GMST1} + \lambda \quad (1.4)$$

The resulting system is the apparent equatorial system of the date of observation.

Aberration

Before transferring the coordinates into a standard system, the effect of annual aberration has to be compensated. This effect is due to the motion of the earth around the sun and the resulting displacement of the apparent position of the observed object.

In classical Newtonian physics, two velocities add to each other linearly. As the Earth moves around the sun with a velocity vector \mathbf{V} , the apparent place of a star \mathbf{p}_1 will be shifted from its true place \mathbf{p} because the two vectors sum up. The Newtonian expression for this effect called annual aberration is:

$$\mathbf{p}_1 = \frac{\mathbf{p} + \mathbf{V}/c}{|\mathbf{p} + \mathbf{V}/c|} \quad (1.5)$$

This expression is in agreement with special relativity to the order of $V/c \propto \mathcal{O}(1 \text{ mas})$, being exact enough for the purpose as described in this work. The difference vector between \mathbf{p} and \mathbf{p}_1 has to be subtracted from the measured source position (Seidelmann et al., 1992, pp. 127).

Aside from this annual aberration, there are other components due to the rotation of the observer around the center of the Earth, the motion of the solar system in the space and more, but these effects are small enough to be ignored in this work.

Mean equinox and equator

The main contribution to the motion of the Earth's rotation axis can be separated into two components: The precession and the nutation. Both are caused by the forces of the solar system's bodies, mostly the Sun and the Moon, on the Earth.

The main contribution to the precession is the lunisolar precession, which moves the mean pole of the equator around the pole of the ecliptic at a period of 26,000 years.

The equator's mean pole is the rotation axis around which the true pole of the equator moves at various, much shorter periods in the order of days to years (Seidelmann et al., 1992, pp. 99).

To transform equatorial coordinates from the mean equinox and equator with coordinates \mathbf{r}_0 to the true equinox and equator of date with the vector \mathbf{r} , the nutation matrix \mathbf{N} can be used (Seidelmann et al., 1992, pp. 109):

$$\mathbf{r} = \mathbf{N}\mathbf{r}_0 \quad (1.6)$$

The nutation matrix can be written as

$$\mathbf{N} = \begin{bmatrix} 1 & -\Delta\psi \cos \epsilon & -\Delta\psi \sin \epsilon \\ +\Delta\psi \cos \epsilon & 1 & -\Delta\epsilon \\ +\Delta\psi \sin \epsilon & +\Delta\epsilon & 1 \end{bmatrix} \quad (1.7)$$

with

$$\begin{aligned} \Delta\psi &= -0^\circ.0048 \sin(125^\circ.0 - 0^\circ.05295d) - 0^\circ.0004 \sin(200^\circ.9 + 1^\circ.97129d) \\ \Delta\epsilon &= +0^\circ.0026 \cos(125^\circ.0 - 0^\circ.05295d) + 0^\circ.0002 \cos(200^\circ.9 + 1^\circ.97129d), \end{aligned} \quad (1.8)$$

d being the number of days from 2451545.0 and

$$\begin{aligned} \epsilon_0 &= 23^\circ 26' 21''.448 - 46''.8150 T - 0''.00059 T^2 + 0''.001813 T^3 \\ \epsilon &= \epsilon_0 + \Delta\epsilon. \end{aligned} \quad (1.9)$$

Here T is defined as

$$T = (JD - 2451545.0)/36525. \quad (1.10)$$

To transfer the aberration-corrected coordinates into the more general system of the mean equinox and equator, where the short periodic motions are ignored, the nutation has to be eliminated. This can be achieved by inverting Eq. 1.6:

$$\mathbf{r}_0 = \mathbf{N}^{-1} \mathbf{r} \quad (1.11)$$

Precession

With the nutation being eliminated, the source coordinates are transferred into the system of the mean equinox and equator of a given epoch ϵ_F with a vector representation \mathbf{r}_0 . This can now be transformed into a standard epoch ϵ_D like J2000.0 with the vector \mathbf{r}_D by using the precession matrix \mathbf{P} (Seidelmann et al., 1992, pp. 99):

$$\mathbf{r}_D = \mathbf{P}[\epsilon_D, \epsilon_F] \mathbf{r}_0 \quad (1.12)$$

$$\mathbf{P} = \begin{bmatrix} \cos z_A \cos \theta_A \cos \zeta_A & -\cos z_A \cos \theta_A \sin \zeta_A & -\cos z_A \sin \theta_A \\ -\sin z_A \sin \zeta_A & -\sin z_A \cos \zeta_A & \\ \sin z_A \cos \theta_A \cos \zeta_A & -\sin z_A \cos \theta_A \sin \zeta_A & -\sin z_A \sin \theta_A \\ +\cos z_A \sin \zeta_A & +\cos z_A \cos \zeta_A & \\ \sin \theta_A \cos \zeta_A & -\sin \theta_A \sin \zeta_A & \cos \theta_A \end{bmatrix} \quad (1.13)$$

with the accumulated precession angles of table 1.1 and the times

$$\begin{aligned} T &= (JD(\epsilon_F) - JD(\epsilon_0))/36525 \\ t &= (JD(\epsilon_D) - JD(\epsilon_F))/36525. \end{aligned} \quad (1.14)$$

The resulting rectangular coordinate vector can be transformed back into spherical coordinates by inverting equation 1.1 to get ra and dec of the epoch ϵ_D .

Table 1.1.: Accumulated precession angles for the base epoch $\epsilon_0 = \text{J2000.0}$ (Seidelmann et al., 1992, p. 104).

ζ_A	$= (2306''.2181 + 1''.39656 T - 0''.000139 T^2) t + (0''.30188 - 0''.000344 T) t^2 + 0''.017998 t^3$
z_A	$= (2306''.2181 + 1''.39656 T - 0''.000139 T^2) t + (1''.09468 + 0''.000066 T) t^2 + 0''.018203 t^3$
θ_A	$= (2004''.3109 - 0''.85330 T - 0''.000217 T^2) t + (-0''.42665 - 0''.000217 T) t^2 - 0''.041833 t^3$

1.2.4. Optical properties

The principal assembly of a radio telescope's focusing system is very similar to that of an optical reflector telescope. A paraboloid primary mirror collects the radiation and focuses it. As the wavelengths in the radio regime are in the order of millimeters to meters and thus much longer than those of light, the diameters of radio telescopes have to be scaled appropriately not to lose directional sensitivity (see Sect. 1.2.4). The resulting mirror surfaces compromise between resolution and size. Another result is the large aperture compared to optical telescopes, to keep the systems as a whole as short as possible.

Near the focal point, the radiation is either directly fed to the detector, or a secondary mirror redirects it back to the primary mirror before. Both cases are well known from optical telescopes, the first type being similar to the "Newtonian" configuration but lacking the planar secondary mirror as the feed is placed directly above the dish. The second type can be laid out in several variations, depending on the position of the secondary mirror and the focal point (Rohlfs & Wilson, 2000, pp. 145), as shown in Fig. 1.6.

Wave optics

To understand the optical properties of a radio telescope, the properties of the radiation that it deals with have to be understood. Like optical light, radio radiation can be described as electromagnetic wave by using the four Maxwell equations:

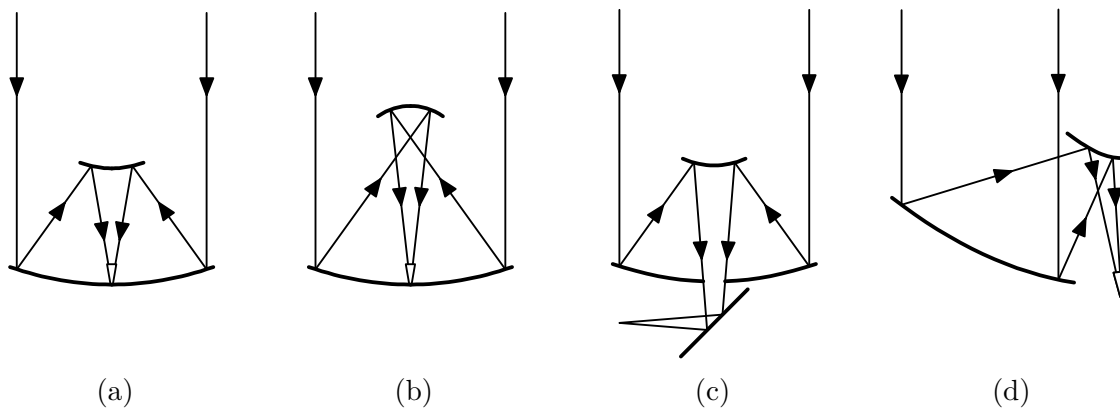


Figure 1.6.: Four different layouts of radio telescope optics. (a) shows the geometry of a Cassegrain system, (b) of a Gregory system, (c) of a Nasmyth telescope and (d) of an offset-Cassegrain system (modified after Rohlfs & Wilson (2000, p. 147)).

$$\begin{aligned}
\nabla \cdot \mathbf{D} &= 4\pi\rho \\
\nabla \cdot \mathbf{B} &= 0 \\
\nabla \times \mathbf{E} &= -\frac{1}{c}\dot{\mathbf{B}} \\
\nabla \times \mathbf{H} &= \frac{4\pi}{c}\mathbf{J} + \frac{1}{c}\dot{\mathbf{D}}
\end{aligned} \tag{1.15}$$

In these equations, \mathbf{E} is the electric field density, \mathbf{D} is the electric displacement, \mathbf{B} is the magnetic induction and \mathbf{H} is the magnetic field density. ρ is the electric charge density which describes the distribution of charged matter interacting with the electromagnetic field, and \mathbf{J} is the electric current density (Rohlf's & Wilson, 2000, pp. 16).

For the description of electromagnetic waves, it is convenient to reformulate the Maxwell equations as wave equations:

$$\begin{aligned}
\nabla^2 \mathbf{H} &= \frac{\epsilon\mu}{c^2}\ddot{\mathbf{H}} + \frac{4\pi\sigma\mu}{c^2}\dot{\mathbf{H}} \\
\nabla^2 \mathbf{E} &= \frac{\epsilon\mu}{c^2}\ddot{\mathbf{E}} + \frac{4\pi\sigma\mu}{c^2}\dot{\mathbf{E}}
\end{aligned} \tag{1.16}$$

Here, σ is the conductivity, ϵ is the permittivity and μ is the permeability. All three parameters have been assumed to be constants in time and space for simplification of the deviation.

An electromagnetic wave propagates through the space and transports energy. This energy flux can be expressed by the Poynting vector \mathbf{S} :

$$\mathbf{S} = \frac{c}{4\pi}\mathbf{E} \times \mathbf{H} \tag{1.17}$$

The direction dependent sensitivity of an antenna is described by the power pattern $P(\theta, \phi)$:

$$P(\theta, \phi) = |\langle \mathbf{S} \rangle| . \tag{1.18}$$

Here, θ and ϕ are the two spherical coordinates. θ is the angle between the z -axis and the pointing vector, and ϕ is the angle between the x -axis and the pointing vector's projection onto the x - y -plane. $P(\theta, \phi)$ describes both the directional sensitivity and its absolute amplitude. If the absolute sensitivity is not important, the normalized power pattern can be used instead (Rohlf's & Wilson, 2000, pp. 127):

$$P_n(\theta, \phi) = \frac{1}{P_{\max}}P(\theta, \phi) . \tag{1.19}$$

To calculate the beam pattern of a circular aperture as it can be found on most radio telescopes, the parameters θ and ϕ can be substituted by a single parameter u by using the rotation symmetry. u is defined as $\sin\theta$. It can be shown that for this system, the normalized beam pattern is described by

$$P_n(u) = \left[\frac{2J_1(\pi u D/\lambda)}{\pi u D/\lambda} \right]^2 = \Lambda_1^2(\pi u D/\lambda) \tag{1.20}$$

with $\Lambda_1(u) = 2J_1(u)/u$ and J_1 being the Bessel function of order one.

In this case, the full half power beam width is

$$\text{HPBW} = 1.02\frac{\lambda}{D} \tag{1.21}$$

with the wavelength λ and the telescope's diameter D (Rohlfs & Wilson, 2000, pp. 139).

Since the wavelength λ is inversely proportional to the frequency f , a real beam pattern $A_{f_1}(\theta, \phi)$ measured at the frequency f_1 is assumed to scale with the HPBW when transferred to another frequency f_2 . The new pattern can be calculated as being

$$A_{f_2}(\theta, \phi) = A_{f_1} \left(\frac{f_1}{f_2} \theta, \frac{f_1}{f_2} \phi \right) . \quad (1.22)$$

The expressions are only capable to describe circular apertures. In reality, a radio telescope has a support structure over the primary mirror which holds the secondary mirror or a feed horn in place. This will affect the shape of the beam pattern by introducing features which are not rotationally symmetrical either, as is shown in Sect. 2.7. It is also possible that the dish loses its circular shape by the deformation under its own weight. This also causes modifications of the beam pattern which need to be corrected for.

Electromagnetic waves are not fully described by the propagation direction and the wavelength. As can be seen in the Maxwell equations, the electric and magnetic fields are represented as vectors themselves. This leads to another degree of freedom which is called polarization.

A general electromagnetic wave propagating along the z -axis has to be described as a linear combination of two individual waves:

$$\begin{aligned} E_x &= E_1 \cos(kz - \omega t + \delta_1) \\ E_y &= E_2 \cos(kz - \omega t + \delta_2) \\ E_z &= 0 . \end{aligned} \quad (1.23)$$

If the difference $\delta = \delta_1 - \delta_2$ is zero or π , the wave is polarized linearly. If it is an uneven multiple of $\pi/2$, the wave in x -polarization is at its maximum if the wave in y -polarization is zero. In combination, the electric field vector spins around the z -axis. Such a wave is polarized circularly if additionally $E_x = E_y$. If the phase difference is in between these values, the resulting radiation has a combination of linear and circular polarization.

The polarization of an electromagnetic wave can be described by the Stokes parameters (Rohlfs & Wilson, 2000, pp. 33):

$$\begin{aligned} S_0 &= I = E_1^2 + E_2^2 \\ S_1 &= Q = E_1^2 - E_2^2 \\ S_2 &= U = 2E_1E_2 \cos \delta \\ S_3 &= V = 2E_1E_2 \sin \delta . \end{aligned} \quad (1.24)$$

The parameter $S_0 = I$ is the total intensity of the radiation. $S_1 = Q$ describes the linear polarization along the x - and y -axis. $S_2 = U$ does the same but for axes rotated by 45° . The parameter $S_3 = V$ gives information about the circular polarization. If $V > 0$, the wave is polarized right-handed. If $V < 0$, it is polarized left-handed respective to the propagation direction.

These equations only apply for monochromatic waves. They can be generalized to describe radiation with a finite frequency interval as it is measured by a real instrument. The Stokes parameters for quasi-monochromatic waves can be expressed in the following form (Rohlfs & Wilson, 2000, pp. 42):

$$\begin{aligned} S_0 &= I = I(0^\circ, 0) + I(90^\circ, 0) \\ S_1 &= Q = I(0^\circ, 0) - I(90^\circ, 0) \\ S_2 &= U = I(45^\circ, 0) - I(135^\circ, 0) \\ S_3 &= V = I(45^\circ, \frac{\pi}{2}) - I(135^\circ, \frac{\pi}{2}) . \end{aligned} \quad (1.25)$$

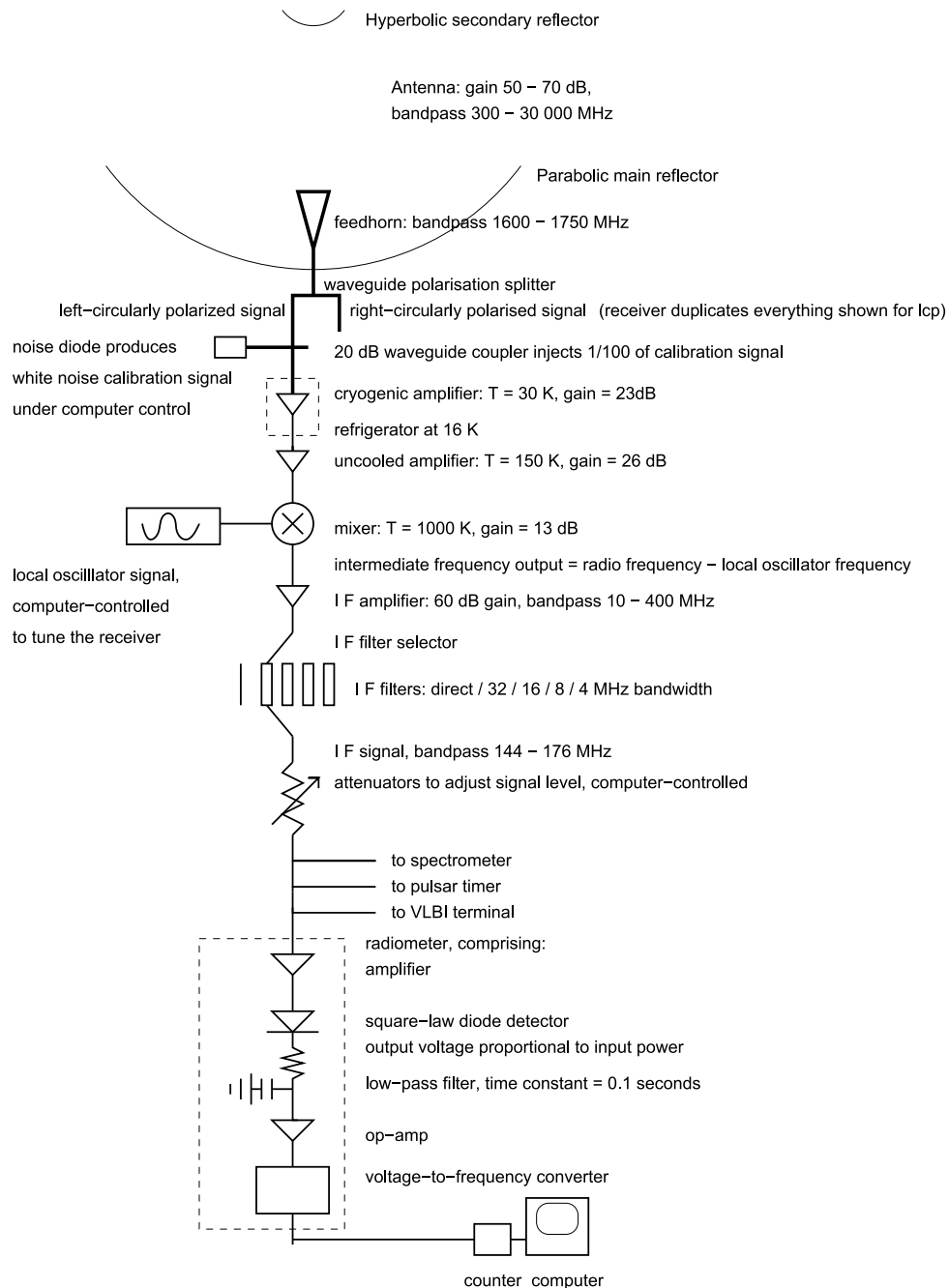


Figure 1.7.: The scheme of a typical receiver's electronics layout (Source: Gaylard (2012)).

This formulation is very useful because it depends on directly observable variables, the intensities of the individual polarization components of the wave.

1.2.5. Receiver systems and signal processing

After the radiation is focused by the optics, it enters the feed horn, a small horn antenna, where it is guided into the receiver electronics. A scheme of a radio receiver is shown in Fig. 1.7.

At the beginning of the electronics chain, the signal is split into its polarization components which are analyzed separately. Afterwards, it is amplified and filtered in several steps and transformed into a signal with a voltage proportional to the input power. This can be measured by converting it into an AC voltage with a frequency proportional to the voltage and then

measuring the oscillations with a counter. The result is a count rate value proportional to the signal's power.

As the amplifiers are not guaranteed to be stable over time, a noise source which emits a constant signal is placed directly after the feed horn. Its signal can be fed into the electronics chain. Variations in the amplification factor will also affect the signal of the noise diode and hence the instabilities can be corrected (Rohlfs & Wilson, 2000, pp. 68).

As described in Rohlfs & Wilson (2000, pp. 133), a brightness distribution $B_\nu(\theta, \phi)$ leads to a total power per unit bandwidth W which can be set into relation to the antenna temperature T_A

$$W = kT_A . \quad (1.26)$$

This is the temperature of a resistor which would emit the same noise power as the observed source when measured with an ideal receiver.

However, the measured antenna temperature does not only consist of the pure signal of the astronomical source which is observed. In a medium like the Earth's atmosphere with a total opacity of τ in the line of sight and an effective temperature T_{Atm} , the signal of the source $T_b(0)$ is absorbed partially, but the atmosphere adds another term:

$$T_A = T_b(0)e^{-\tau} + T_{\text{Atm}}(1 - e^{-\tau}) . \quad (1.27)$$

The parameters T_{Atm} and τ introduce the complicated physics of the atmosphere into the measurement (Rohlfs & Wilson, 2000, pp. 186).

As described before, the measured signal is amplified several times. The amplifiers, cables and other electronics all add noise to the signal of the antenna. As the signals of the source and atmosphere, the noise contribution can be expressed as temperature. The total measured system temperature T_{sys} is a sum of all these parts:

$$T_{\text{sys}} = \sum T_i . \quad (1.28)$$

It can be shown that the fundamental limit for the receiver resolution in terms of system temperature is

$$\frac{\Delta T}{T_{\text{sys}}} = \frac{1}{\sqrt{\Delta f \tau}} . \quad (1.29)$$

Here, Δf is the total receiver bandwidth and τ is the integration time (Rohlfs & Wilson, 2000, pp. 61). This equation gives the resolution of an ideal receiver. It is impossible to build a receiver with a better resolution.

1.3. The 26 m Hartebeesthoek radio telescope in detail

The Hartebeesthoek 26 m radio telescope (Fig. 1.8) is an equatorially mounted Cassegrain reflector telescope. It is located at $25^\circ 53' 14''.4$ South, $27^\circ 41' 05''.2$ East in a valley at a distance of 65 km from the city of Johannesburg in South Africa.

The primary dish has a diameter of 25.9 m and an aperture of $f/D = 0.424$. The surface accuracy measures 0.5 mm rms. It is equipped with receivers ranging from $\lambda = 1.3$ cm up to $\lambda = 18$ cm wavelength. The full details of the receivers are listed in table 1.2.

Table 1.2.: The receiver characteristics of the Hartebeesthoek 26 m radio telescope¹.

Band	18 cm	13 cm	6 cm	4.5 cm	3.5 cm	2.5 cm	1.3 cm
Feed horns	1 x circular	1 x circular	2 x diagonal	1 x diagonal + parallel-plate polarizer	2 x circular	1 x circular	1 x circular
Polarization	LCP & RCP	LCP & RCP	LCP & RCP	LCP & RCP	LCP & RCP	LCP & RCP	LCP & RCP
Amplifier	cryogenic HEMT	cryogenic HEMT	cryogenic HEMT	cryogenic HEMT	cryogenic HEMT	uncooled PHEMT	uncooled
Standard frequency [MHz]	1666	2280	5000	6670	8580	12180	23000
Lower frequency limit [MHz]	1608	2210	4650	6008	8180	12048	22000
Upper frequency limit [MHz]	1727	2450	5200	6682	8980	12216	24000
Receiver bandwidth [MHz]	120	240	400	660	800	168	2000
Beam width (FWHM) [deg]	0.494	0.332	0.160	0.113	0.092	0.059	0.033
Beam width between first minima [deg]	1.19	0.80	0.36	0.32	0.23	0.16	0.073

Source: http://www.harttrao.ac.za/hh26m_factsfile.html



Figure 1.8.: The 26 m Hartebeesthoek telescope (Source: http://www.hartrao.ac.za/gallery/hart_26m+moon_070628.jpg).

The telescope is part of the TANAMI (Tracking Active Galactic Nuclei with Austral Milliarc-second Interferometry) program, a Very Long Baseline Interferometry (VLBI)-collaboration of radio observatories on the southern hemisphere (Müller et al., 2010).

For the VLBI-observations, a lot of calibration observations were recorded during the last years. An extensive part of these data has not been analyzed for astrophysical content but only served for instrument calibration to date.

The aim of this work is to provide a software package for automated analysis of these data by extracting the flux densities of each observed source and calibrate them using standardized calibration files.

This approach provides a user friendly possibility to take a look into the huge data sets. By the objective analysis it gives insight into instrument specific features.

The extraction methods take advantage of the theoretical discussions of the last sections. In the following chapters, the analysis process is explained in detail and the function of the software is described. Then an exemplary analysis of the source PKS 0637-752 is presented and problems are discussed. Finally, an outlook for further refinement of the software is given.

2. The analysis of radio data

The aim of this work is to develop an automated analysis tool for extensive sets of single-dish observation data from the 26 m Hartebeesthoek telescope as described in Sect. 1. In this chapter, the layout and function of this software is described. First, the input data is presented, followed by details of the analysis methods and calibration requirements. The capabilities of the software are discussed in Sect. 3.

2.1. Scanning strategies and coordinate systems

As described in Sect. 1.2.4, a radio telescope is not able to take spatially resolved pictures but it measures all the radiation which enters into the beam pattern. To determine the flux of a quasi-point like source, as many astronomical objects are, the receiver outputs of at least two positions have to be compared: on-source and off-source. This makes it possible to subtract the background radiation from the signal given by the source of interest.

This on-/off strategy requires precise pointing of the antenna so that the source is reliably at the maximum of the beam pattern in on-position.

This requirement can be dropped by a certain amount when more than two positions are used, such that the spatial signal distribution itself will give information about the pointing relative to the source.

A common way to do this is to scan across the sources in various angles and offsets. The resulting signal vs. coordinate curves are sections through the PSF convolved with the source's

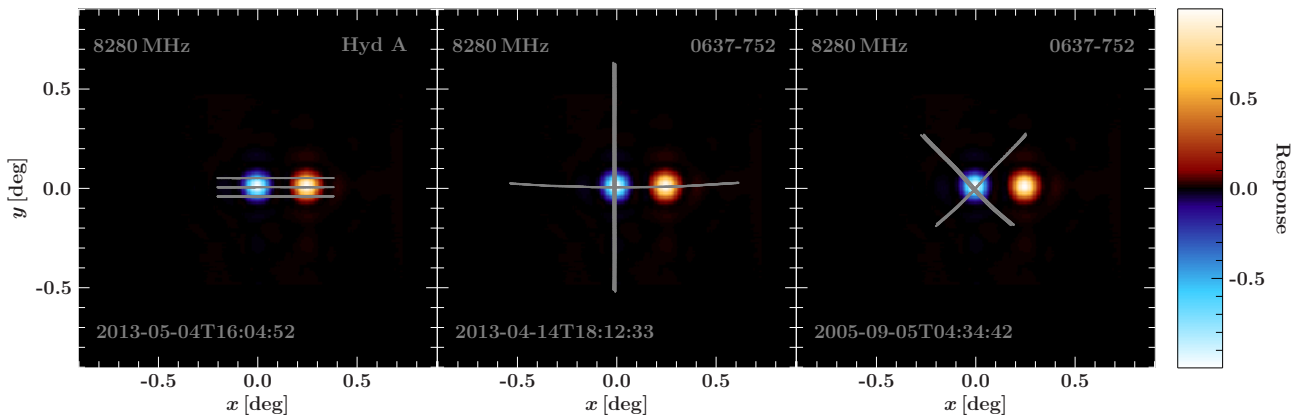


Figure 2.1.: Three different scan layouts. The coordinates (x, y) are spherical coordinates, centered on the source position. Color coded is the assumed point source convolved with the total PSF. The leftmost, called a “drift”-scan, is composed of three lines with fixed declination. They are obtained by using the earth’s rotation to drift the telescope’s beam across the source for three different offsets. The scan in the center is a “cross”-scan which probes the source in both directions while the telescope is driven by motors. The rightmost is also a cross-scan but angled against the coordinate system by 45° . In all three cases, the telescope was operated in “Dicke switched” mode, which turns on a second detector. Its signal is subtracted from the first one, resulting in a second, negative PSF portion.

spacial flux density distribution. When we regard point sources, the flux density distribution is a delta peak at the source position, so the signal curve becomes a section through the telescope's PSF itself. Figure 2.1 shows different scan layouts. In the following, every path over the source is called a "subscan", and all subscans of an observation together form one "scan".

A scan composed of three parallel subscans or two subscans angled against each other while crossing near the center of the beam pattern contains information of the exact position of the point source. With this parameter known, the amplitude of the signal can be reconstructed by scaling the height of the PSF to match the signal curves, if the background can be subtracted properly.

In Sect. 1.2.4 the deformation of the mirror dish and thus the PSF was discussed. For an analysis of scan data as described above, it is essential to find a good model for the beam pattern, at every position on the sky. This requires to take the coordinate dependent deformation of the PSF into account if it is in measurable order of magnitude. At the time of the beginning of this work, the deformation of the 26 m telescope has not been known, so the software has to be designed in a most flexible way to include this feature.

Here the equatorial mount of the telescope becomes important. The PSF is fixed to the orientation of the optical components of the telescope which move in the equatorial system (ra, dec). The deformation of the mirror is caused by gravity. This force aligns with the zenith-vector which is described in the alt-azimuthal coordinate system (az, el). Both coordinate systems do not align, which makes the beam pattern depend on four coordinates.

2.2. The input data format

Each observation data set to be analyzed with the pipeline as presented in the following sections is required to be a Flexible Image Transport System (FITS)-file (Wells et al., 1981) with at least 5 extensions:

- Primary extension
- Frontend extension
- Calibration extension
- Subscan extension(s)
- Chart record extension

The primary extension contains information about the target object and subscan information. The frontend extension describes the detector used for the following data set. The calibration extension is the 0th subscan extension. It gives a time series of count rates with about the half being recorded with the calibration noise diode turned on, while the rest shows only the background signal. The following extensions contain the actual subscan data over the source. The count rates in both polarization channels are associated with the respective time (MJD) and coordinate values in several systems such as J2000, B1950 equatorial coordinates as well as alt-azimuthal coordinates. The last extension contains a chart for the whole scan as well as the system temperatures.

The data format is specified in detail in Gaylard & Buchner (2003).

2.3. General analysis pipeline layout

The purpose of the analysis pipeline as discussed in this work is to analyze extensive batches of Hartebeesthoek Radio Astronomy Observatory (HartRAO)-data files at once without the need of manual input. On the other side, a maximum of flexibility in terms of manual control was favored, to be able to reanalyze difficult data sets or to take advantage of new calibration data without having to run the whole pipeline from the beginning.

These requirements lead to the following design aspects:

- The general language is C. The CFITSIO-library (Pence, 2010) is used for file handling. The MPFIT-library (Markwardt, 2009) is used for data fitting.
- The pipeline is broken down to smaller sub-programs for individual tasks.
- The sub-programs are able to work either in series for automated data reduction or on their own if manual control is required or they are to be used in other data pipelines.
- There is the possibility to manually check the quality of each fit. Therefore, standard plots are generated during the data reduction. These are created using the PGPLOT-library (Pearson, 2011).
- For calibration file handling a Calibration Database (CALDB) is used.
- For flux calibrator file handling a calibration source observation database is used.
- For data tracking an analysis database is provided.
- For parameter handling the Parameter Interface Library (PIL) is used (Borkowski et al., 2002).

The layout of the resulting pipeline can be seen in Fig. 2.2. The input data file is scanned for all information relevant to the analysis.

The core of the data reduction is the fit of a model composed of a function representing the beam of the telescope, and a linear background for each scan, to the data. Therefore, the CALDB is searched for the best-matching PSF, which is represented by a FITS-image.

After the fit, the uncertainties are estimated by probing the χ^2 -landscape. At this point, the original data are parameterized sufficiently for further analysis, so the input data file is closed and the next step of the pipeline begins.

The value of interest is the flux density of the observed source, measured in Jansky (Jy). This observable can be obtained by comparing the amplitude of the signal of the source with that of a calibrator source. Preconditions are that the amplitude is measured in a comparable unit, and that the calibrator source flux is known to good accuracy. Sect. 2.9 summarizes the different steps of the calibration process.

Necessary for all sub-programs is an environment variable `SDA_PATH` which points to the directory where all analysis and calibration files are stored in sub-folders.

In the following sections the individual parts and aspects of the pipeline are discussed in detail.

2.4. The calibration database

Data analysis of this kind requires some sort of calibration information. In the case of the pipeline presented in this work, this can be split into three topics:

1. Telescope coordinates

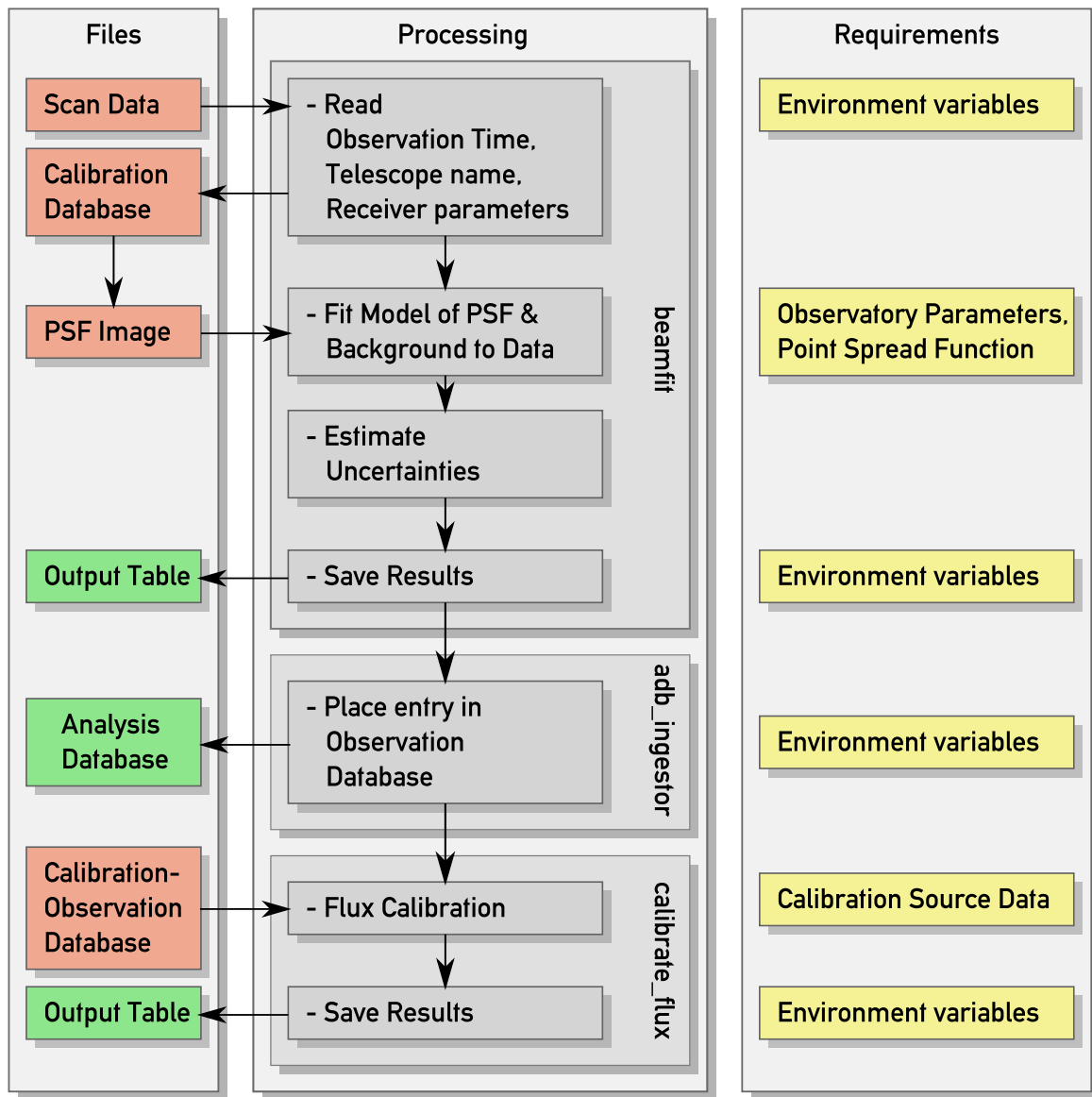


Figure 2.2.: The layout of the data analysis pipeline. On the left hand side, the file layer is shown (red: input, green: output). In the middle, the data and processing flow is described. The boxes at the right hand side illustrate the required information for the processing steps.

2. Telescope beam pattern
3. Flux calibrator information

The coordinates of the telescope are essential for the alt-azimuthal coordinate system set-up. The beam pattern is required as part of the model. The flux calibrator files are analyzed observations of celestial sources themselves for which the flux density is known.

As the requirements and handling of flux calibrator files are different to those describing the telescope parameters, the calibration files are split. The CALDB therefore lists only files which belong to the points 1 and 2. Flux calibrators are listed in a separate database described in Sect. 2.9.

The CIF

The CALDB for the analysis program described here is based on the HEASARC CALDB as described in George et al. (1998). It consists of a central Calibration Index File (CIF), a

FITS-file binary table which lists the available calibration files. If requested, a special calibration file can be searched for in this file by using the Extended Filename Syntax (Pence, 1999). If there is more than one file matching to the requirements, the latest one before the given validity date is returned by the routines.

The definition of the CIF binary table is given in Appx. A.1.

Software is provided to ingest and remove calibration data files. This is described in Appx. A.2.

2.5. The fit

It has been shown that the output signal of the receiver is a mixture of the source signal and of “background” noise produced by the atmosphere, the receiver electronics and other unwanted side effects. To extract the astronomical signal, the different signal components are modeled and fitted to the data.

The fit reduces the amount of data from several hundreds of data points to very few numbers characterizing the scans, and is supposed to find the interesting properties.

The characterization is accomplished by the introduction of a model M which represents the theoretical composition of the signal and by determining its “best-fit”. This is the parameter vector for which the model describes the data points optimally for a given statistic theory. A diagram of the fitting loop is shown in Fig. 2.4.

The model

As discussed in Sect. 1.2, the signal detected from a point source while scanning over it should resemble a section through the telescope’s PSF, which may be influenced by the coordinates the dish is pointing at. In Sect. 2.7, the analysis of the beam is described and it is obvious that the distortion of the PSF shape due to gravity is hard to detect.

To avoid confusion, in this section the presence of the two polarization channels is not marked explicitly in each step. However, until the flux calibration is accomplished, each step in the analysis including the model fit is done independently in both channels.

The evaluation of the PSF-component in the fit is a linear interpolation between the pixels of the beam image, which can be used as an analytically defined function f_{PSF} . If there is no matching PSF for the frequency the data was recorded in, another one is used, scaled according to eq. 1.22. The coordinate look-up is done using the WCS-functions (Mink, 1997). This is done in a “beam-intrinsic” coordinate system (x, y) . This system is obtained by rotating a spherical coordinate system which is initially aligned to the equatorial system first in ra , then in dec to the telescope’s pointing direction. In this system, the PSF is of constant shape, aside from the gravitational deformation. In single beam mode, the PSF-component of the model at the source coordinates $x(ra, dec)$, $y(ra, dec)$ is then defined as

$$M_{\text{PSF}}(ra, dec) = A_1 \cdot f_{\text{PSF}}(x(ra, dec), y(ra, dec)) . \quad (2.1)$$

If the second beam is switched on (mode “Dicke switched”), f_{PSF} has to be evaluated at two points. The model part is then defined as:

$$M_{\text{PSF}}(ra, dec) = A_1 \cdot f_{\text{PSF}}(x(ra, dec) + x_{\text{off}}, y(ra, dec)) + A_1 \cdot A_2 \cdot f_{\text{PSF}}(x(ra, dec) + dx, y(ra, dec) + dy) . \quad (2.2)$$

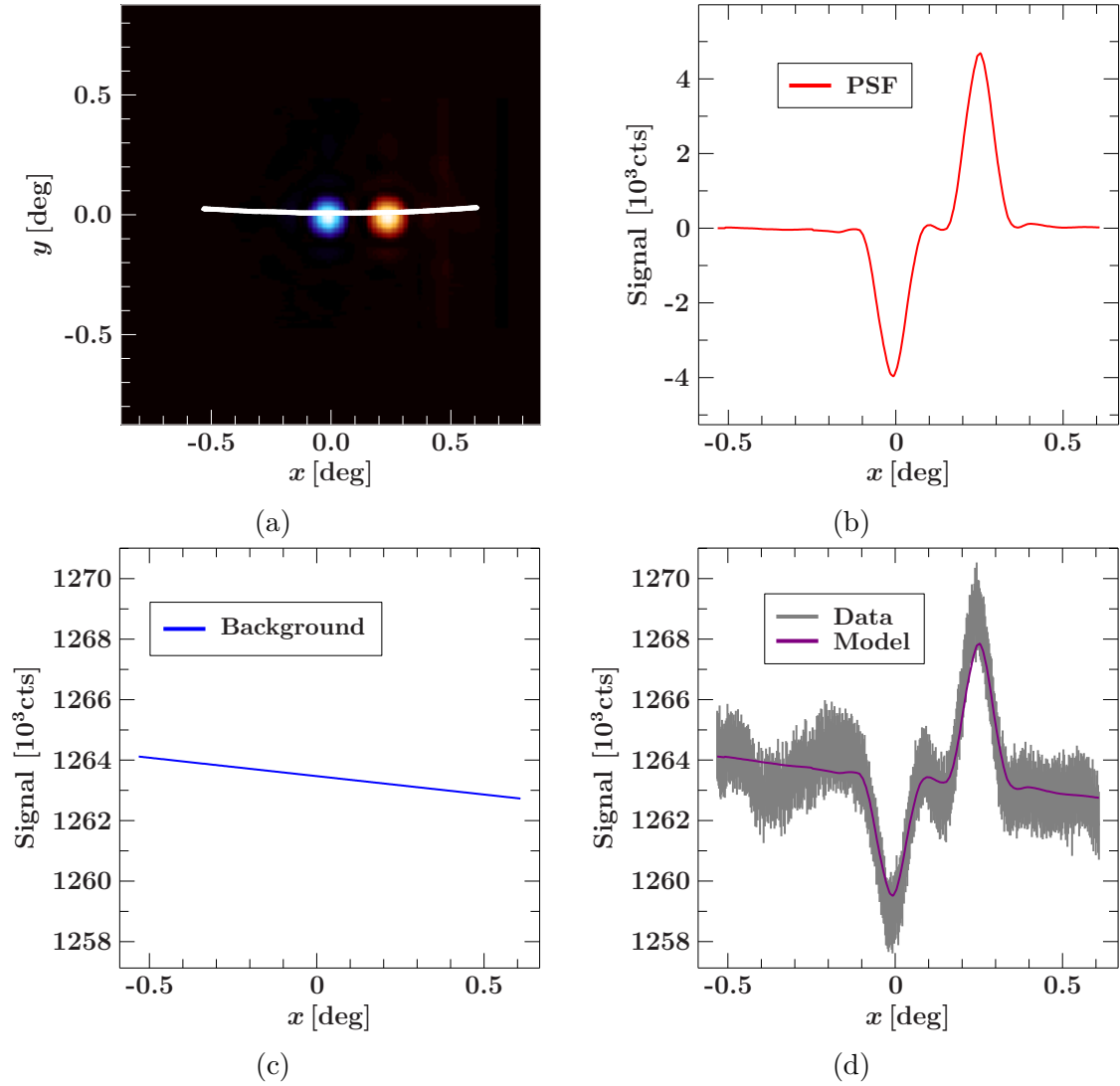


Figure 2.3.: The individual components of the model for one subscan and one polarization channel. The subscan coordinates are transformed into the beam intrinsic coordinate system (a). At these points, the two-dimensional PSF model is evaluated and scaled in amplitude (b). This is combined with a linear function depending on the angular distance of the individual data points to the start of the subscan (c). The resulting best-fitting model for this subscan is shown in (d).

Here, x_{off} is the distance between the two beams, dx and dy are small pointing corrections to allow shifting the beams relatively to each other, and A_2 is the amplitude factor of the second beam (initially set to -1).

The other part of the signal is called “background” in the following. It contains system noise as well as ground pick-up from the sidelobes of the PSF or signals of other sources if they are near to the pointing direction (Rohlfs & Wilson, 2000, p. 61). It is not possible to model all background effects physically correct, so a simplified model is introduced. It consists of a linear background in each scan and polarization channel, which is proportional to the angular distance between the starting coordinate of the scan and the actual data point.

The angular distance α between the recent pointing (ra, dec) and the start of the subscan (ra_0, dec_0) is

$$\alpha(ra, dec) = \arccos(\sin(dec) \cdot \sin(dec_0) + \cos(dec) \cdot \cos(dec_0) \cdot \cos(ra_0 - ra)) . \quad (2.3)$$

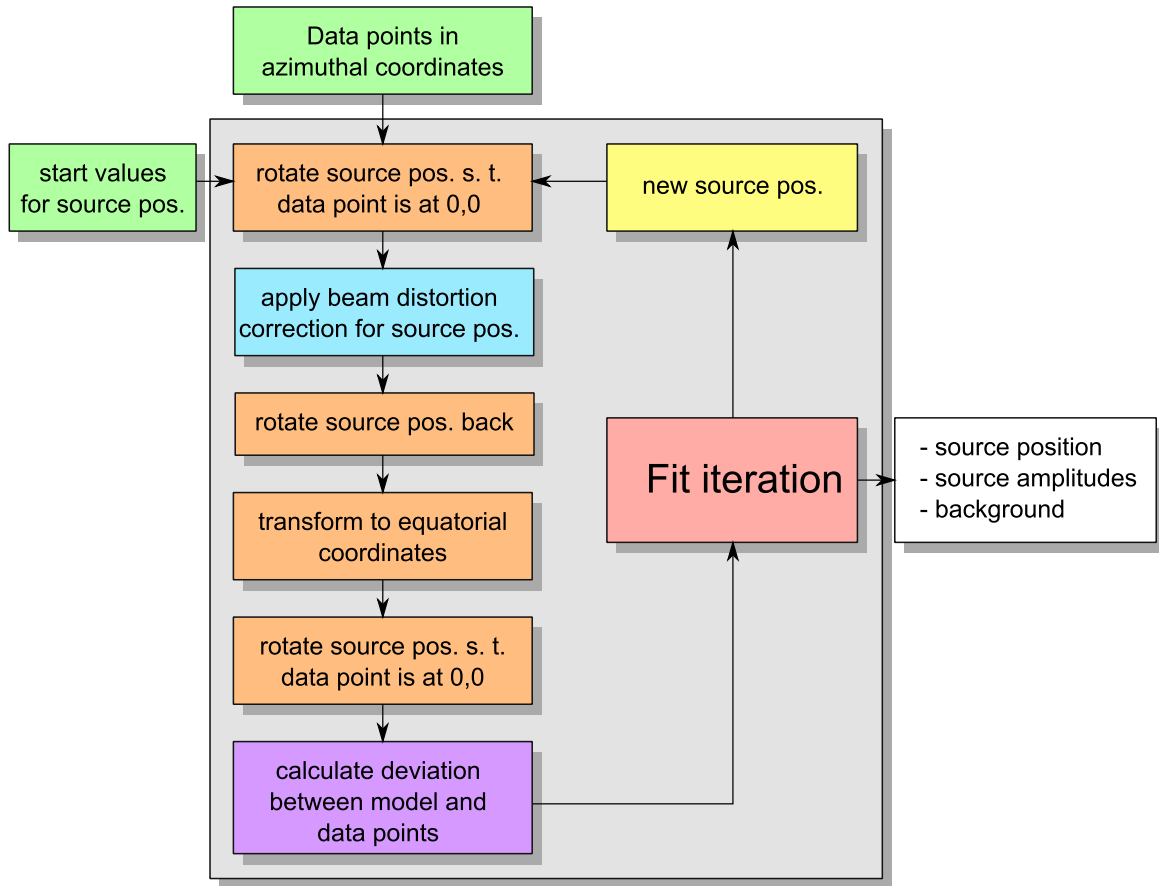


Figure 2.4.: A scheme of the fitting loop. The data points and start values for the model are the input for the iterator (green). In each loop, multiple time-dependent coordinate transforms have to be calculated (orange) to make the beam distortion correction possible (blue). The end of each cycle is marked by the calculation of the data-model-deviations (purple) and the use of MPFIT (red) for the determination of the next set of model parameters (yellow). If the accuracy or abort conditions are fulfilled, the final set of parameters is returned (white).

The background model of subscan n is defined as

$$M_{Background}(ra, dec) = C_n + L_n \cdot \alpha(ra, dec) . \quad (2.4)$$

This is a compromise between flexibility to account for fluctuations and simplicity to avoid overparameterization of the model in regions which are not interesting for the following analysis. Fig 2.3 shows the individual model components for an example subscan. However, there are cases in which the measured background can not be described by this model in a proper way.

The total flux density of the model in the direction (ra, dec) is given by

$$M(ra, dec) = M_{PSF}(ra, dec) + M_{Background}(ra, dec) \quad (2.5)$$

In the case that a relation between the pointing direction and the beam distortion is known, the model can be extended with an optional function to alter the effective source position relatively to each data point, with the pointing position in azimuthal and equatorial coordinates as parameters. The coordinate transform procedure which is necessary for this task is described in the following.

Beam distortion correction

A technical problem of large radio telescopes is that not only the mount has to support the telescope's weight, but also the dish of the primary mirror has to withstand gravity. As the construction is not fully rigid, the mirror will inevitably deform a bit under its own weight. This of course also alters the telescope's PSF. The software as described in this paper has to be able to correct for this deformation of the beam pattern.

As described in Sect. 1.3 and 2.1, the axes of the equatorial mount of the Hartebeesthoek 26 m telescope are not aligned with the gravitational forces they have to counter. This makes additional coordinate transforms necessary. The beam pattern of the telescope is bound to the structural components and is thus best described in the equatorial system. On the other side, the gravitational force will deform the pattern according to the dish's orientation in alt-azimuthal coordinates, and it must be assumed that at least a part of the deformation follows these coordinate axes.

At the launch of the program, the coordinates of the data points are read-in in the J2000 equatorial system. Afterwards, they are converted into the alt-azimuthal system by using the HartRAO-own coordinate system C-functions to ensure compatibility to the existing programs. The theoretical background for these coordinate transformations is described in Sect. 1.2.3.

Then the deformation correction is handled by mimicking the data acquisition process in the fitting loop (see Fig. 2.4). Each data point's position is the pointing direction of the telescope to the time of its recording. The assumed source position gives the relative coordinate at which the PSF has to be evaluated. For the distortion correction, these relative coordinates have to be manipulated in the alt-azimuthal system. Therefore, the following steps are executed in each iteration, for each data point:

1. The assumed source position (az, el) is rotated in alt-azimuthal coordinates, such that the data point is at $(0, 0)$. The source coordinates in this system are (u, v) .
2. In this new system, the distortion correction can be accomplished by manipulating the assumed source position. The transformation can be dependent of (ra, dec, az, el) . This leads to new effective source coordinates (u_{eff}, v_{eff}) .
3. The resulting, effective coordinates are rotated back into the alt-azimuthal system. These coordinates (az_{eff}, el_{eff}) are transformed into equatorial J2000 coordinates. This leads to the representation (ra_{eff}, dec_{eff}) .
4. The assumed effective source position is rotated into a data point-centered system again. In this system, the beam pattern has its natural representation and the new coordinates (x_{eff}, y_{eff}) take the place of (x, y) in equations 2.1 - 2.5.
5. The PSF is evaluated at the assumed source position.

It has to be noted that it is not correct to transform the data point coordinates into a source-centered coordinate system instead of steps 1 and 4. While it would be comfortable to have all data points in a common system in which the PSF is constant in position and deformation corrected, this approach is impossible because of the nature of spherical coordinate systems, as Fig. 2.5 illustrates. In Cartesian coordinates this coordinate system could be constructed because of the existence of translation vectors. In spherical coordinates, coordinate transforms have to be calculated by using rotations instead. The matrix which is used for a rotation of this kind changes its coordinate representation, making a common coordinate system for our problem impossible.

The user interface of the implementation of the fitting procedure is described in Appx. A.3. Information about the output file of the program is given in Appx. A.4.

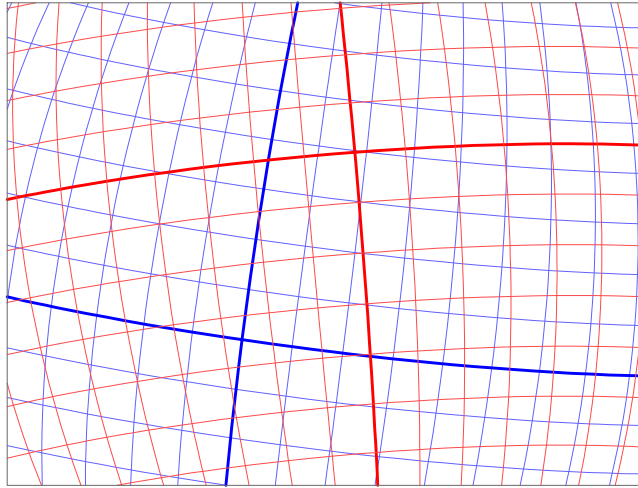


Figure 2.5.: Two spherical coordinate systems (red: A, blue: B) rotated relatively to each other in ϕ - and θ - direction. The bold lines represent the prime meridians and equators. The thin lines represent the isolines in 5° -steps. It is obvious that the origin points of the two systems ($(0,0)_A$ and $(0,0)_B$) can not be shifted to the other respectively by using a common “translation vector”, which is a major difference to Cartesian coordinate systems. In contrast, the coordinates of $(0,0)_A$ as seen in the the system B differ from the coordinates of $(0,0)_B$ as seen in the the system A by more than the sign.

2.6. Uncertainty estimation

To be able to describe the uncertainties of the parameters, Lampton et al. (1976) give a good insight into χ^2 -based error estimation. With the assumption of χ^2 -distributed data points, the results of this paper which aims specifically on X-Ray data analysis can be used for radio astronomy data reduction, too.

The idea behind the estimation of the uncertainty Δp of a single model parameter p with a best-fit value p^0 is the strong dependence of the probability, that the real value of p lies inside the interval $]p^0 - \Delta p, p^0 + \Delta p[$ to the difference between the goodness at the best-fit value $\chi^2(p^0)$ and at the borders of the interval, $\chi^2(p^0 \pm \Delta p)$. Here, $\chi^2(p^0 \pm \Delta p)$ have to be calculated by freezing p but fitting all other free parameters.

Lampton et al. (1976) have shown that the value $\Delta\chi^2 = \chi^2(p^0 \pm \Delta p) - \chi^2(p^0)$ is a direct indicator for the significance and confidence of the fitted parameter value. For the 1σ -confidence interval, $\Delta\chi^2$ is exactly 1.

By probing the χ^2 -landscape around the best-fit value, the 1σ -uncertainty can be found.

This idea is implemented in `beamfit`. The `calc_uncert`-variable can be used to turn on this option. Then, after the final model is found, each parameter is varied until the value of $\Delta\chi^2$ is found to a predefined accuracy or the maximum number of iterations is reached. For each new value, the model is fitted again with this parameter frozen, and the new χ^2 is analyzed.

The initial value for Δp is the 1σ -error estimate from MPFIT. In the first iteration, the resulting initial value of $\Delta\chi^2$ is used to find the new value of Δp . This is done by assuming that each side of χ^2 can be described as a parabola centered around p^0 and running through Δp_{\pm} . This parabola is defined uniquely and can be used to find the next estimate for Δp_{\pm} . After the first iteration, the secant method is used to find the new values.

Additionally to the search for $\Delta\chi^2 = 1$, the parameter `calc_chisq_cuts` enables to save one-dimensional sections of the χ^2 -landscape along each parameter axis.

Similar to this one-dimensional probing of the goodness parameter, Lampton et al. (1976) describe how this can be extended to two parameter values. They show that the confidence intervals of two-parameter variations differ to those of the case discussed above. The 1σ -contour corresponds to $\Delta\chi^2 = 2.3$.

As a typical model of the analysis as described in this work has about 20 parameters, there are several hundred possible two-parameter contours. It is not only impractical to examine such numbers of contours for several thousands of observations, it also costs a lot of calculation time. Because of this, `beamfit` only has the option to calculate a map of the χ^2 -landscape for one possible parameter combination at a time. This can be enabled by the parameter `calc_chisq_landsc`, the resulting map is saved as FITS-image. See Sect. A.3 for a description of the PIL-parameters.

2.7. Measurement of the PSF

As explained in Sect. 2.5, it is essential to have a good description of the telescope's PSF. Therefore, a series of calibration scans in "map"-mode is analyzed.

In this mode, the telescope scans over a bright source in many lines, like the electron beam of a cathode ray tube TV over the screen. Here, the source itself probes the PSF. A scan over Tau A at 1668 MHz can be seen in fig. 2.6.

To get a model of the PSF, images are constructed from these data sets. Therefore, the coordinates of the data points are rotated exactly as described for the fit itself (see Sect. 2.5). As target position, the literature value of the observed source is assumed. Thus, the resulting coordinates are in an appropriate system for re-evaluation during a fit.

After the coordinates are transformed, the maximal side lengths of a rectangular box orientated parallelly to the coordinate axes can be fitted into the scans. This box is the outline of the image which will be produced in the following three steps.

First, the image area is divided into pixels with centers at (x_p, y_p) . The number and size of the pixels is calculated using the desired image resolution provided by the user.

Second, along each subscan, a cubic spline provided by the Gnu Scientific Library (GSL) is set up to interpolate between the data points. These functions are evaluated at the centers of the rows (y_p) or columns (x_p) of the picture, depending on the orientation of the subscans.

In the third step, these points are used as sampling points for a second set of cubic splines, this time connecting between the subscans. The image is obtained by evaluating these splines at the pixel coordinates (x_p, y_p) .

The picture array now contains an approximated view of the sky around the calibration source as it would be seen in a picture, as if the radio telescope had an imaging detector.

As the data does not only contain the signal of the source, the background has to be subtracted. Therefore, the signal in test areas in the corners of the picture was examined. A background which depends linearly on x and y is approximated and subtracted.

The final steps are to find the maximum value of the PSF. As the interest is to find a model for the beam, it is appropriate to normalize the pixel values such that the maximum is 1. Then the coordinate center is shifted by a small correction offset to get the maximum to $(x = 0, y = 0)$. As the correction is very small (e.g., on the order of $1^\circ/100$), the coordinate shift can be approximated by a linear vector.

The final image can then be stored in a FITS-image.

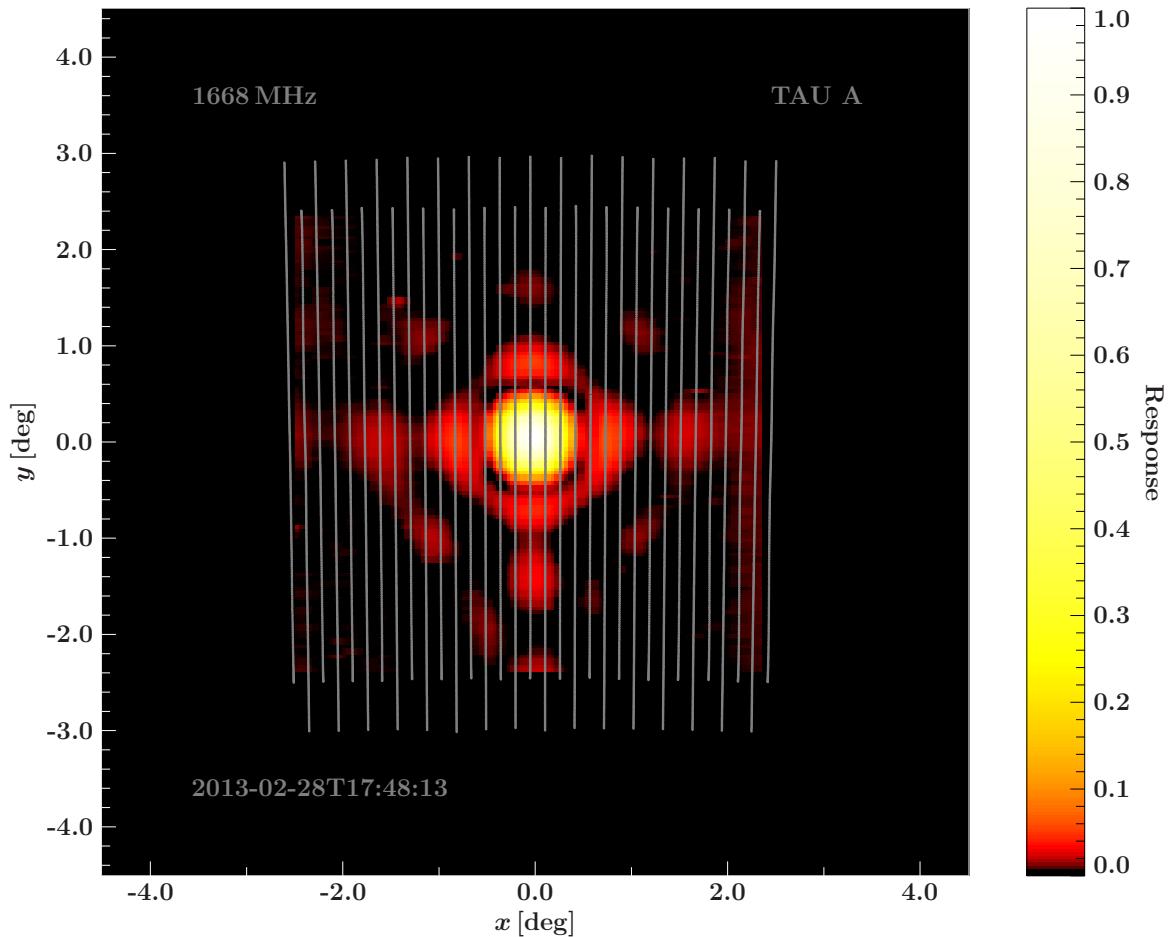


Figure 2.6.: A map scan over Tau A. The gray lines represent the data points of the scan. In the background, the processed map of the PSF in Channel 2 can be seen. The coordinate system is aligned with the source center. A cubic spline is used to interpolate the data points along each subscan and evaluated at the picture's rows. Then a second set of cubic splines is used to interpolate between the individual subsamples and evaluated at the image's columns. The result is stored as a three-dimensional FITS-image, two axes representing the spatial coordinates and the third discriminating between the two polarization channels.

2.8. The analysis database

To keep track of the analysis results, an Analysis Database (ADB) is built up. As the CIF, its central archive is a binary table in a FITS-file. It is described in Appx. A.5.

If a filtered extract of this file is needed, the tool `adbfilter` can be used. Its syntax is described in Appx. A.6.

2.9. Calibration sources and the calibration source database

As already mentioned in Sect. 2.3, the amplitude's primary unit is [Hz]. With the noise diode scan prior to each observation, the output of the counter can be compared to the diode's temperature, which makes it possible to convert the signal's unit to [K]. As the noise diode's radiation strength and temperature is supposed to be constant over weeks and months, this temperature is a good unit for comparisons.

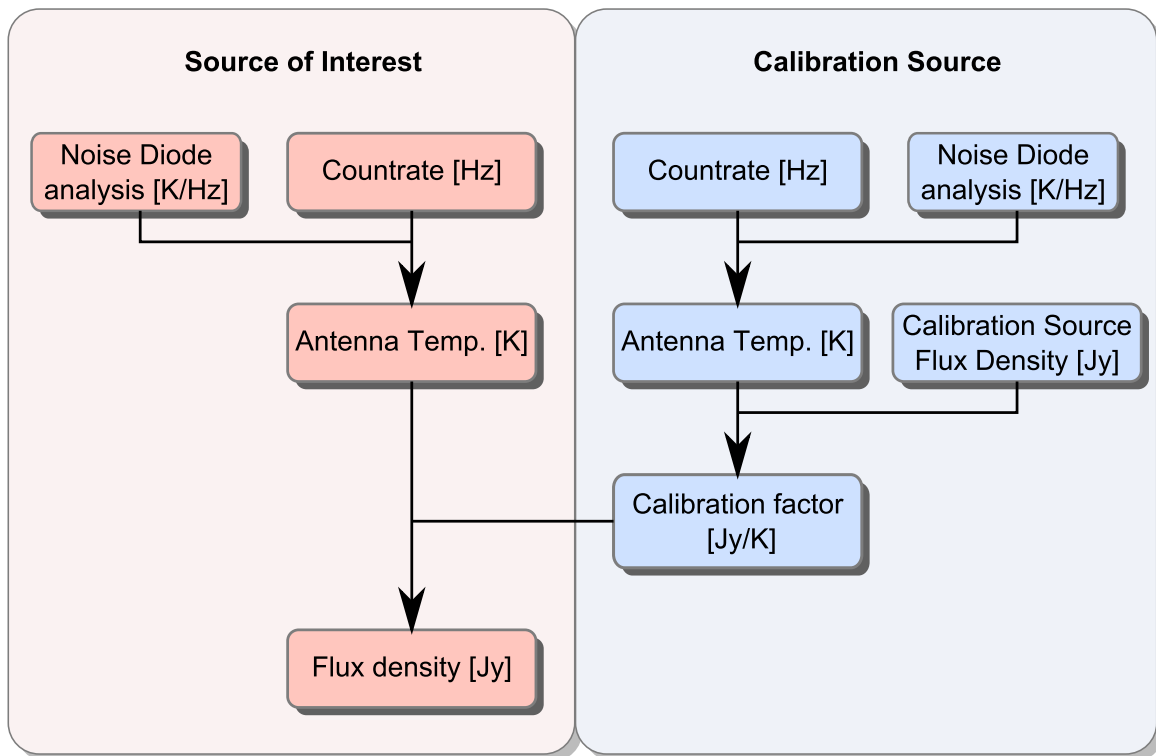


Figure 2.7.: The scheme of the calibration process for one observation. The inability of the telescope to directly measure the flux density of an object requires an additional observation of a calibrator source. Both data sets are analyzed identically with a fit, which gives the signal amplitudes in Hz. A comparison with the noise diode count rates converts these into the antenna temperatures, measured in K. With the calibration source flux density known, a conversion factor can be derived, which finally leads to the source flux density in Jy. This approach makes frequent observations of calibration sources necessary.

However, in most cases the absolute flux density of a source is requested, so a way to convert the temperature into [Jy] is needed.

This can be done by using calibrator sources. These sources are astronomical objects themselves, but with flux densities S_{cal} which are known to be constant over time.

The conversion scheme used for the analysis program as presented in this work is shown in Fig. 2.7.

The basic idea is to take two observations, one of the source of interest and one of a calibration source at about the same time. Both observations have to be recorded at the same frequency and bandwidth and preferably at similar positions on the sky. They are analyzed with the methods as presented in the previous sections.

Both data sets include the count rate-to-temperature conversion factors, so the measured amplitudes are known as temperatures, T for the unknown source and T_{cal} for the calibrator.

Then the calibration source's flux density at the observed frequency and bandwidth are read from an external data base, and the flux density of the other source can be calculated as

$$S = \frac{T}{T_{cal}} \times S_{cal} \quad (2.6)$$

The CSDB

To access the calibration source information, another database is built: the Calibration Source Database (CSDB). Like the ADB and CALDB, it consists of a FITS binary table to list the information, and individual files for each entry.

With the calibration source observation information being individual scan analyses, the CSDB file is very similar to the ADB. It is described in Appx. A.7.

A tool is provided to ingest calibration source observations into the CSDB. It is described in Appx. A.8.

2.10. Flux density calibration

When an analysis shall be calibrated using a the calibration source observations listed in the CSDB, the tool `calibrate_flux_adb` can be used. Its syntax is described in Appx. A.9.

The calibration is done by following the scheme in Fig. 2.7. First, if the observation is recorded in dual-beam mode, the average amplitude for each polarization channel is calculated:

$$A^{l/r} = A_1^{l/r} (1 + |A_2^{l/r}|) / 2 \quad (2.7)$$

The uncertainty propagates:

$$\Delta A^{l/r} = ((1 + |A_2^{l/r}|) \cdot \Delta A_1^{l/r} + A_1^{l/r} \cdot \Delta A_2^{l/r}) / 2 \quad (2.8)$$

The total amplitude in [K] can be derived by using the [K/Hz]-conversion factors $\kappa^{l/r}$ and summing up the two polarization channels, as eq. 1.25 tells:

$$T = A^l / \kappa^l + A^r / \kappa^r \quad (2.9)$$

with an uncertainty of

$$\Delta T = \Delta A^l / \kappa^l + A^l / \kappa^l + A^l \cdot \Delta \kappa^l / (\kappa^l)^2 + \Delta A^r / \kappa^r + A^r \cdot \Delta \kappa^r / (\kappa^r)^2 \quad (2.10)$$

These numbers are calculated for the observed source ($T \pm \Delta T$) and the calibration source ($T_{cal} \pm \Delta T_{cal}$). With the calibrator's flux density known ($S_{cal} \pm \Delta S_{cal}$), T can be converted to S using eq. 2.6. The error propagates and gives a final uncertainty of

$$\Delta S = \frac{\Delta T \cdot S_{cal} + T \cdot \Delta S_{cal}}{T_{cal}} + \frac{T \cdot S_{cal}}{T_{cal}^2} \cdot \Delta T_{cal} \cdot \quad (2.11)$$

The calibration observation used for comparison is selected by the following requirements:

- The keyword **TELESCOP** must match.
- The keyword **FREQ** must match.
- The keyword **BANDWIDTH** must match.
- The calibration observation must lie in the past of the observation to be calibrated.

If more than one calibration observation matches these criteria, the one which is closest in time is chosen.

The output of the flux calibration process is described in Appx. A.10.

3. Analyzing 8 years of PKS 0637-752-data

3.1. The data

As a test of the analysis software, more than 1000 observations of the source PKS 0637-752 have been examined. These data span a time interval of eight years, between 2005 and 2013. Additionally, over 8000 calibration observations of various sources have been analyzed automatically.

In the course of this work, the influence of the gravitational deformation on the shape of the PSF could not be measured. Hence, the distortion correction option of the analysis program has been turned off.

3.2. Beam fitting

The initial step for the analysis is to analyze each data set with the program `beamfit`, as described in Sect. 2.5. For all analyses the same options and parameters have been set. The data range has been limited after the initial fit to remove irrelevant parts of the background. The data point errors have been estimated, assuming Gaussian distribution of the differences between data points and the model. The model parameter uncertainties were estimated by probing the χ^2 landscape. Input files which did not include a complete noise diode scan analysis were ignored.

Fit quality

In the following, four distributions which characterize the fits are presented. Figure 3.1a shows a histogram of the final χ_{red}^2 -distribution of all fits. The distribution is peaked around approximately $\chi_{\text{red}}^2 = 1.7$ with a width of about 0.2.

In Fig. 3.1b, the polarization-averaged countrate measurement of the source signal is illustrated. According to this plot, typical source signals have amplitudes of several thousand counts per second. The distribution exhibits several broad humps which are due to the different source luminosities. However, as the count rate as shown here is only an indirect indicator of the flux density but have to be converted to the antenna temperature for a direct proportionality, the peaks are very broad in this plot.

Two other interesting distributions can be seen in Fig. 3.1c and Fig. 3.1d. The first describes the distribution of the polarization-averaged standard deviation of the residuals of the individual fits. It is centered at approximately 1.3 with a width of around 0.1. The second shows the distribution of the mean residual values of the fits, also averaged over the two polarization channels. It is narrowly centered around 0. This indicates that the fitting routine worked well to minimize the deviations between the model and data points.

Figure 3.2 shows an exemplary drift-scan of Hyd A on 2012-03-14 at a frequency of $f = 8280$ MHz analyzed in this course. While the overall agreement between the data points and the model is

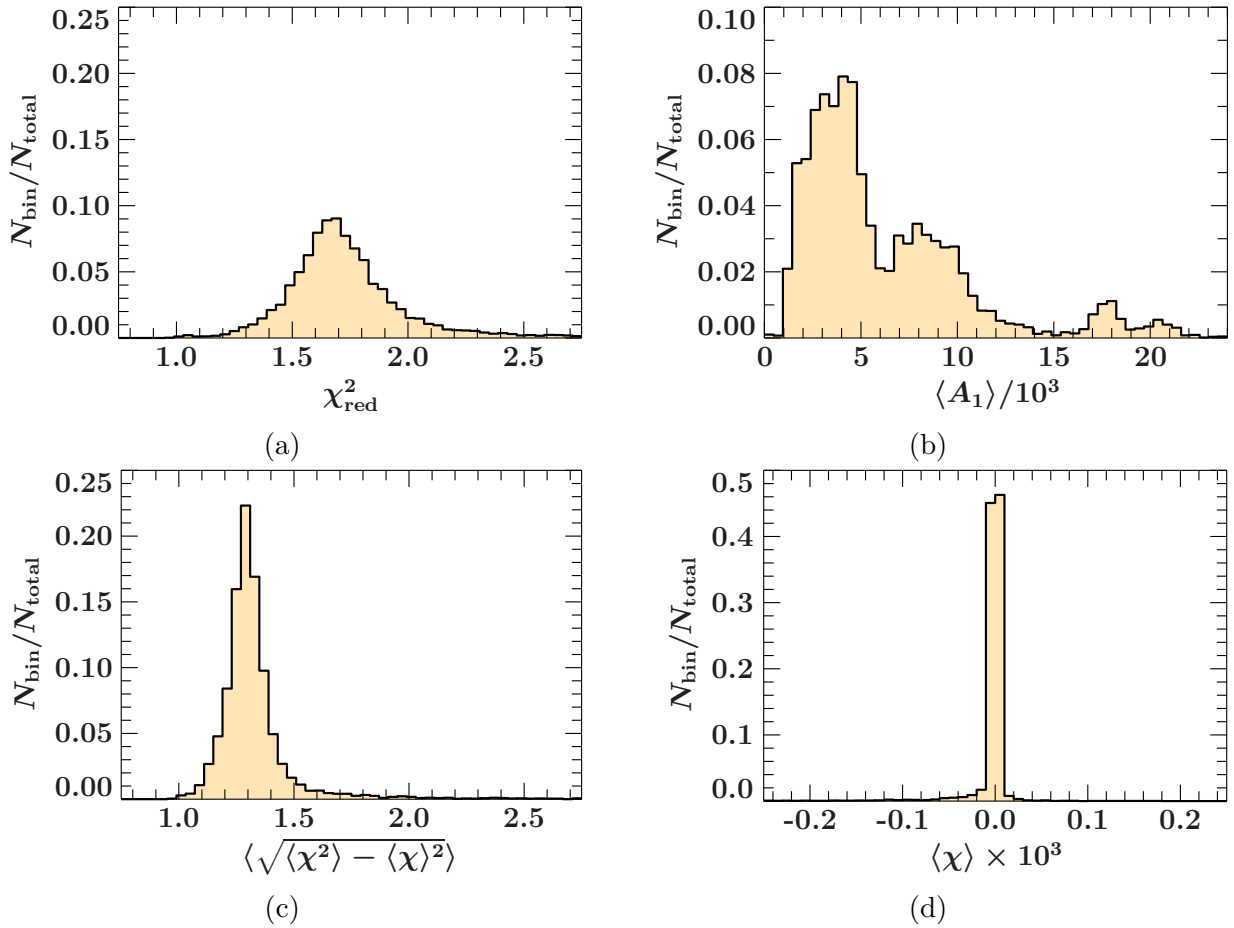


Figure 3.1.: Four different characterizations of the fit results. (a) shows the distribution of the final χ_{red}^2 -values of the fits. (b) illustrates the distribution of the polarization-averaged fit result of the source signal amplitude. It features several humps which are caused by the different source luminosities. (c) shows the polarization-averaged standard deviation distribution of the fit residuals. (d) describes the polarization-averaged mean residual value. It is peaked around 0 which signals that the fitting routine worked well.

good, a first evidence for the point-source assumption being wrong are the residuals in subscans 2 and 3 at the peak positions. However, it might also be the case that these residuals are due to the gravitational deformation of the dish and the resulting beam distortion which has not been corrected for.

Example scans

The histograms do not exhibit severe failures of the fitting routines for most cases. To get a better feeling of the resulting models, two examples are described in the next paragraphs.

Figure 3.3 illustrates a drift-scan over J1939-0637 on 2012-06-07 at $f = 8280$ MHz. The data quality is worse than in the scan of Hyd A. In polarization channel 1, the data of subscans 1 and 3 exhibit severe perturbances. In subscan 1, the linear background model is unable to describe the measured data points and the residuals are high along the whole subscan. In subscan 3, short term disturbances can be seen. However, the fit results are remarkably good, as this observation was later selected to be in the CSDB before the features were known. A detailed examination of the χ^2 -landscape illustrates that the bad data quality causes the declination parameter of the main beam in channel 1 to have two nearby minima, as seen in Fig. 3.4a.

However, this uncertainty has no influence on the best-fit value for the source signal's amplitude, as Fig. 3.4b shows. The perturbances have been compensated by the fact that the model is fitted to all three subscans together.

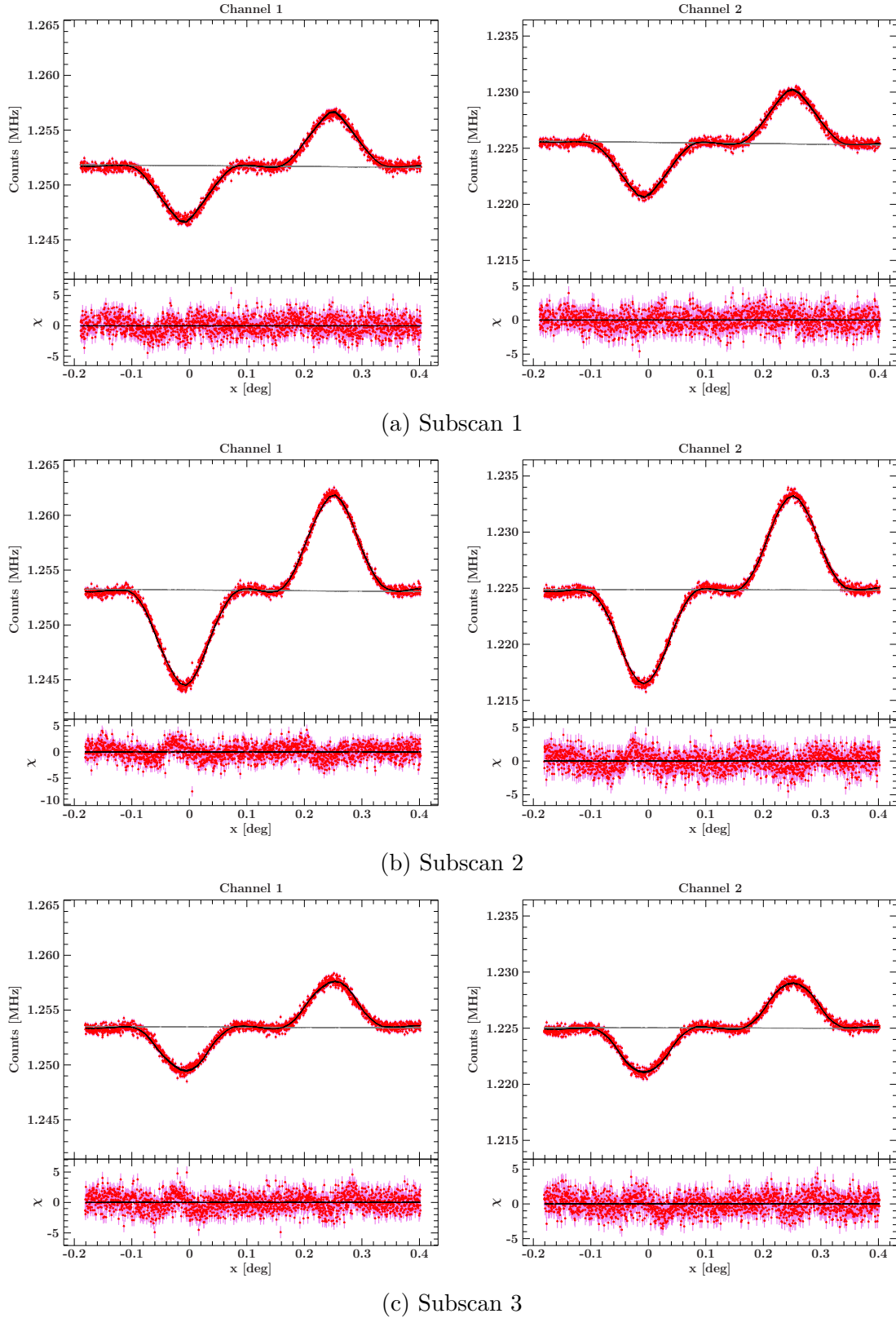


Figure 3.2.: The three subscans of a drift-scan over Hyd A on 2012-03-14 at $f = 8280$ MHz. The data points (red, error bars: pink) are in good agreement with the fitted model (black). The linear background component is shown in gray. In subscans 2 and 3, residuals around the peaks are visible, which are caused by the PSF model measured with Tau A not fitting exactly to Hyd A. Two possible reasons for this are the wrong assumption of the sources being point-like and the influence of the gravitational distortion of the beam pattern.

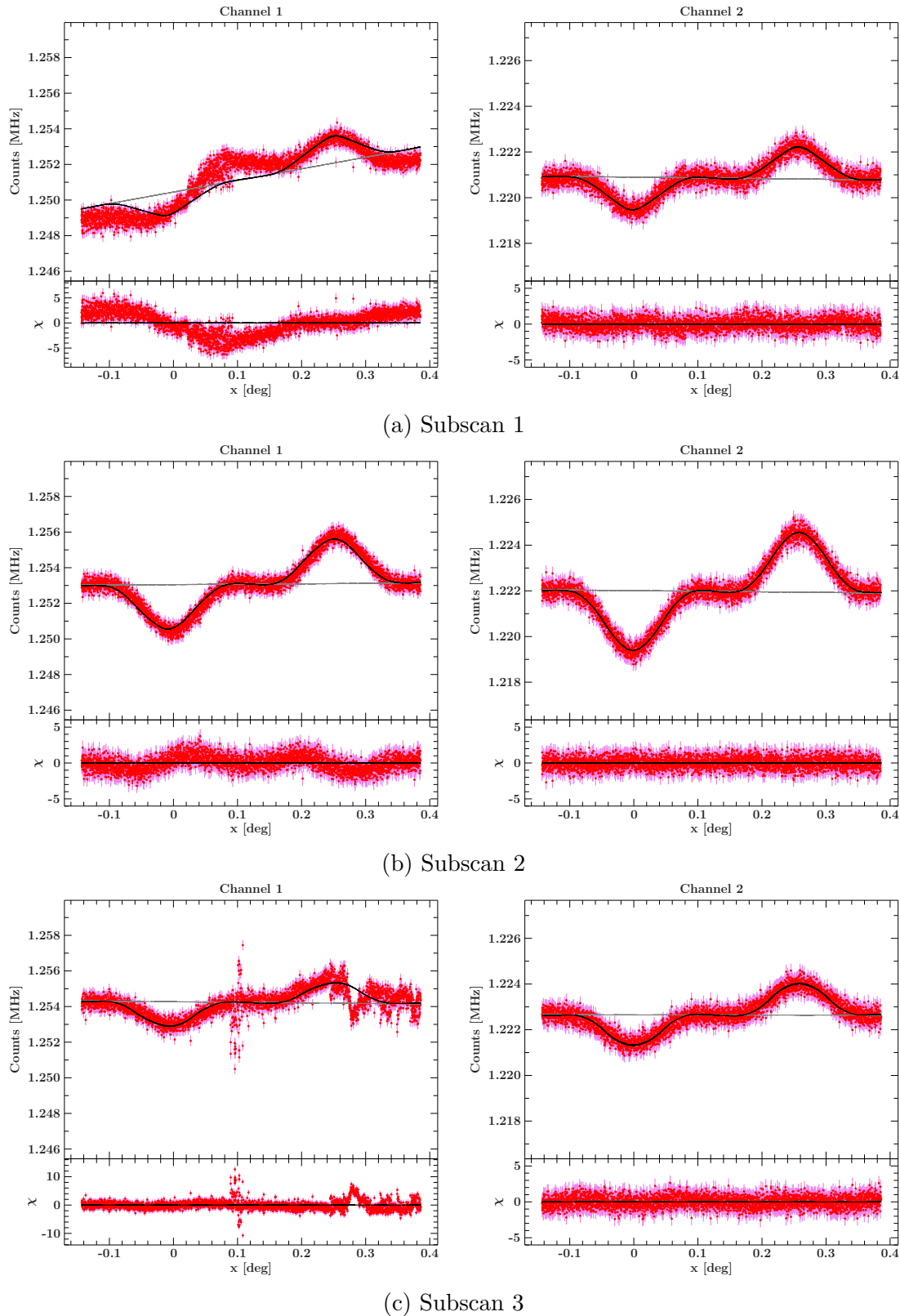


Figure 3.3.: The three subscans of a drift-scan over J1939-0637 on 2012-06-07 at $f = 8280$ MHz. The signal in polarization channel 1 of subscans 1 and 3 shows severe perturbances. In subscan 1, this results in the linear background model being unable to describe the data. However, because the model is fitted simultaneously to all three subscans, it has been possible to fit the beam position successfully. The resulting measurement of the source signal's amplitude is independent of the small possible variations of the problematic dec parameter, as Fig. 3.4 shows.

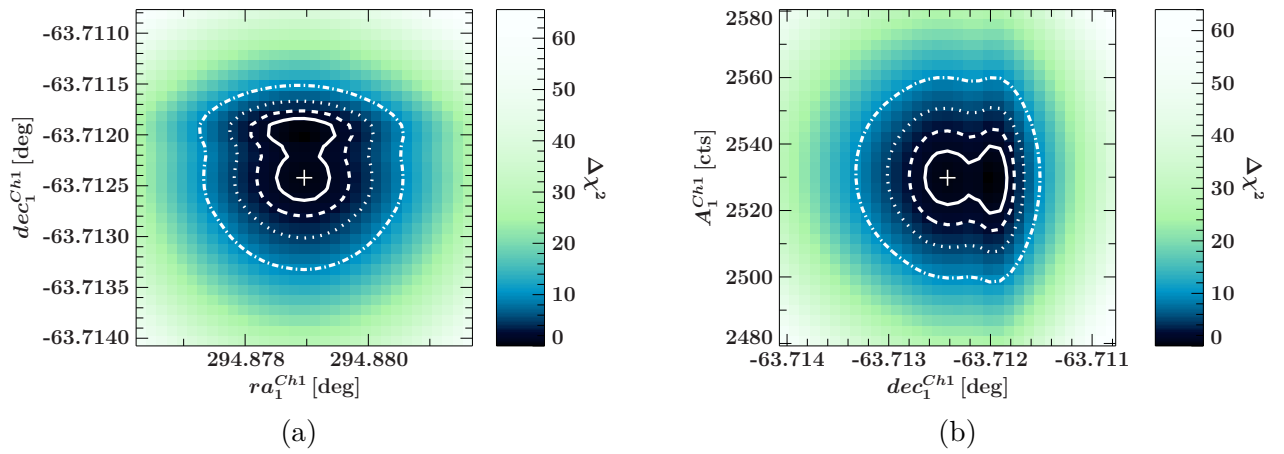


Figure 3.4.: Two two-dimensional χ^2 -landscape sections to the scan shown in Fig. 3.3 in polarization channel 1. Panel (a) describes the dependency between the two coordinates of the beam pattern that is fitted to the data. The χ^2 -valley around the best fit-values (white cross) exhibits two minima spaced apart by about 0.5×10^{-3} deg in declination, perpendicular to the subscan lines. The right ascension parameter is not affected by this feature. Panel (b) shows the same for the declination parameter and the source signal's measured amplitude. The latter is also not influenced by the imprecise measurement of the declination parameter.

3.3. Calibration source data

To set up an initial CSDB, the tool `csdb_ingestor` is used. It is outfitted with an internal calibrator source database, including 14 sources with known radio spectra. The flux density at a frequency f for 13 sources can be calculated by using the formula given by Baars et al. (1977):

$$\log_{10}(S) = a + b \log_{10} \left(\frac{f}{1\text{MHz}} \right) + c \left(\log_{10} \left(\frac{f}{1\text{MHz}} \right) \right)^2 \quad (3.1)$$

The accuracy of this parameterization is described as 5%.

For the source B 1934-638, the formula given by Reynolds (1994)

$$\log_{10}(S) = a + b \log_{10} \left(\frac{f}{1\text{MHz}} \right) + c \left(\log_{10} \left(\frac{f}{1\text{MHz}} \right) \right)^2 + d \left(\log_{10} \left(\frac{f}{1\text{MHz}} \right) \right)^3 \quad (3.2)$$

is used with $a = -30.7667$, $b = 26.4908$, $c = -7.0977$, $d = 0.605334$. He estimates the uncertainty to about 2% of the flux density.

With these calibrator flux values, a total of 4753 calibration source observations at $f = 8280$ MHz are described. These include all available data sets at this frequency, for which the noise diode analysis results were given in the original file and for which the uncertainty estimation converged in 20 iterations while not taking longer than 2 hours per analysis. Based on a random sample it is assumed that the last two criteria filter out the lowest quality scans.

Time evolution of the calibration factor

For a first examination, Fig. 3.5 shows the time evolution of S_{cal}/T_{cal} of all 4753 observations, broken down to the different sources.

This plot reveals several interesting features. First, there is a gap in the data between the second half of 2008 and the first half of 2010. During that time, the telescope was out of service because the main bearing of the telescope's polar shaft failed and had to be replaced (author unknown, 2010).

Second, there are unexpected jumps in the time evolution, one between the end of May and the beginning of August in 2011, and the other after the first half of January in 2013. A lookup in the telescope's logbook brings the reason for these steps: In May of 2011, it was noticed that there was a problem with the control of the secondary reflector focus position, probably related to a malfunction of a readout potentiometer or its wiring. This caused the focus being set to a wrong position, which results in a decrease of the antenna gain, and thus increasing the calibration factor. The faulty parts were repaired on August 4, 2011, resetting the calibration factor to the level before.

At January 7, 2013, four main deflector panels were realigned that had been offset for a single-dish holography project to measure the surface accuracy of the main dish. The newly aligned surface elements improved the quality of the reflector surface accuracy and thus the antenna gain, which reduces the calibration factor (Quick, J., priv. comm.).

There are more features to be seen in this diagram. It is noteworthy that the calibration factors are dependent on the source from which they are calculated. Ideally, all sources should lead to the same calibration factor, which is the justification for the whole calibration strategy. However this is obviously not the case, so an explanation has to be found and a decision is to be made which data should be used as calibration information.

The assumption is that the different calibration factors primarily arise from the sources being not ideal point sources but extended to the limits of the telescope's resolution. Such small deviations from point source-like data will not stand out to the eye but could alter the best-fit value for the amplitude of the source's signal enough to fan out the calibration factor.

Between 2006 and 2008, oscillations in the calibration factors of 3C123 and Hyd A can be seen. A comparison between these oscillations and the annual variation of the sources' angular distance to the Sun demonstrates that the position of the sun relative to the sources might have an influence on the signal, as Fig. 3.6 shows.

A better understanding of the dependencies gives Fig. 3.7, which illustrates the distribution of the calibration factor measurements in relation to the angular distances between the sources and the Sun. It can be seen that the correlation is very broad. The reasons for this widening are long-term variations of the calibration factor which overlay the seasonal oscillation. This makes the influence of the angular distance to the Sun hard to compensate. A correction of this feature has not been implemented for this work.

For an exemplary lightcurve analysis it has been decided to select the source Hyd A as the primary calibrator as it provides a good coverage over the whole time of observation. Also, it is the source that passes closest to the zenith which ensures the least affection by the gravitational deformation of the telescope dish.

From the initial 4753 observations, the best 591 scans of Hyd A have been chosen manually and ingested into the CSDB. Criteria in the selection process have been the χ^2 -value of the fits, the uncertainty estimates as well as the calibration factor of each analysis compared to the whole sample. The selection is a subjective process. The time evolution of the calibration factor as visualized in Fig. 3.8 shows that the resulting curve as a whole follows the trend which is already present in Fig. 3.5. Only outliers are removed which is necessary for a calibration database.

With the same process, CSDBes with the sources 3C123 and J1939-6342 have been built as shown in Fig. 3.9 and Fig. 3.10. With the source 3C123, about the same time coverage can be obtained as with Hyd A. The first available observations of J1939-6342 are located in 2008, so observations before this date can not be calibrated using this calibrator source.

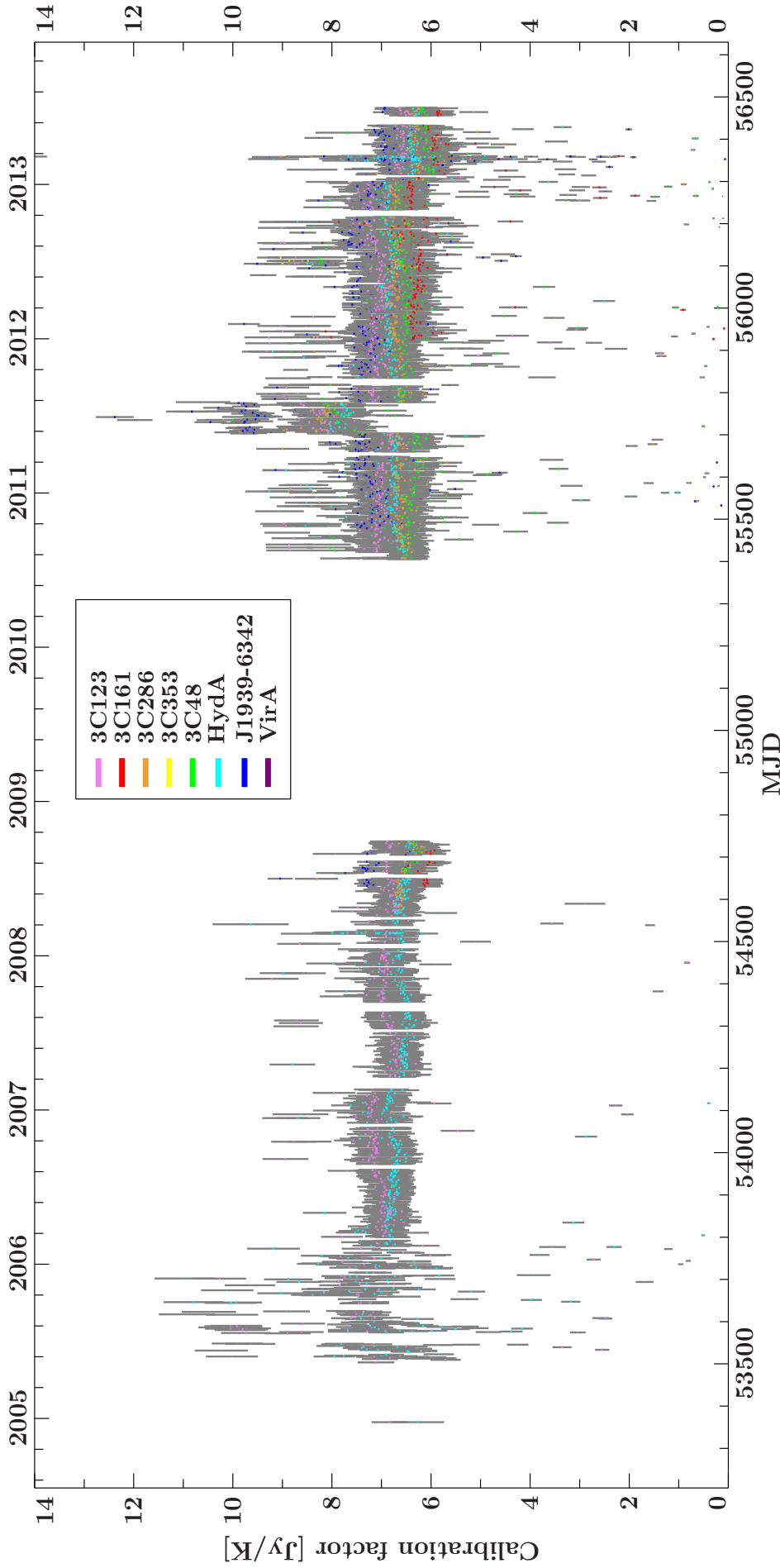


Figure 3.5.: The time evolution of the S_{cal}/T_{cal} -calibration factor for all available calibration source observations at $f = 8280$ MHz. Color coded are the individual sources. The error bars are all in gray for clarity. Between the second half of 2008 and the first half of 2010, no data points are available due to the malfunction of the main bearing of the telescope's polar shaft (author unknown, 2010). Note also the steps in the calibration factor between the end of May and the beginning of August, 2011, and after the first half of January in 2013. These steps are caused by realignments of focusing elements of the telescope, which lead to a change in the gain and thus in the calibration factor.

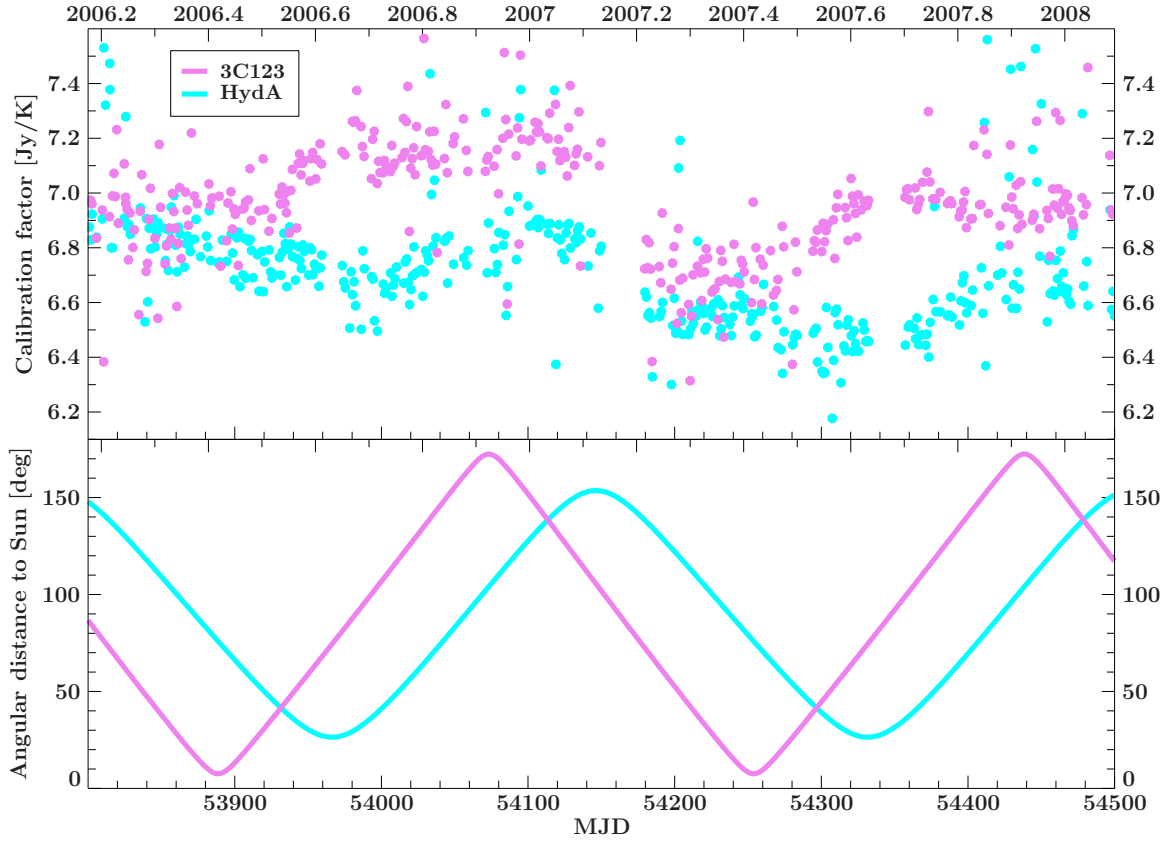


Figure 3.6.: The time evolution of the calibration factor S_{cal}/T_{cal} of 3C123 and Hyd A in comparison to the angular distances of the sources to the Sun. Period and phase shift similarity between the curves lead to the assumption that the Sun's position in relation to the pointing direction influences the measured signal. The periodic oscillation of the calibration factors is combined with a long-term variation, leading to an overall decrease of S_{cal}/T_{cal} in the depicted time interval. Error bars are not shown in this figure for clarity reasons.

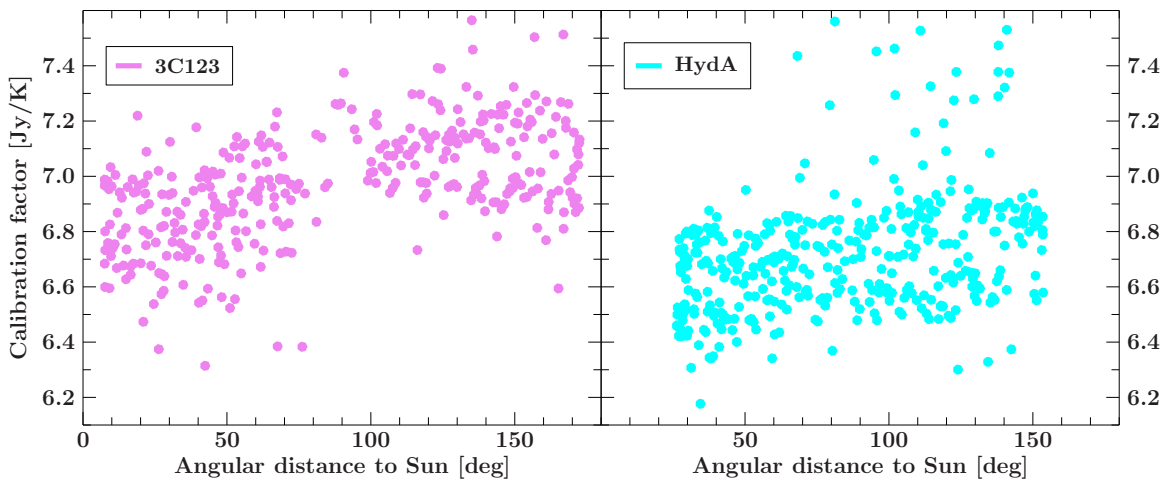


Figure 3.7.: The dependence of the calibration factor S_{cal}/T_{cal} of 3C123 and Hyd A on the angular distances of the sources to the Sun is demonstrated in this plot. A correlation can be seen in this plot, but as the non-periodic part of the time variation is not compensated, the distribution is very wide. As in Fig. 3.6, error bars are not shown in this plot.

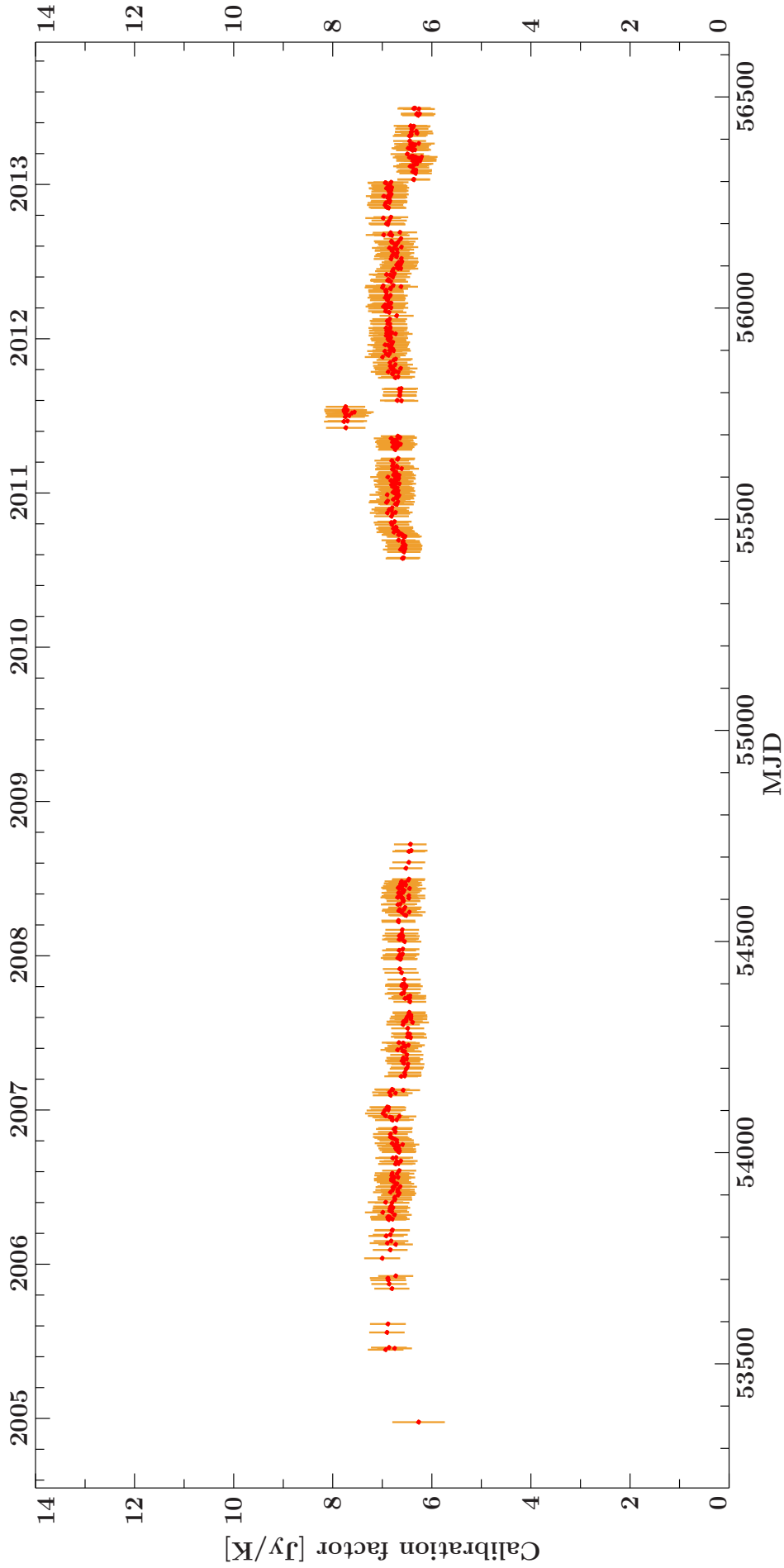


Figure 3.8.: The time evolution of the calibration factor S_{cal}/T_{cal} of the selected observations of Hyd A. This source gives a good coverage over the whole time range. The steps in the antenna gain can be seen clearly again in this plot.

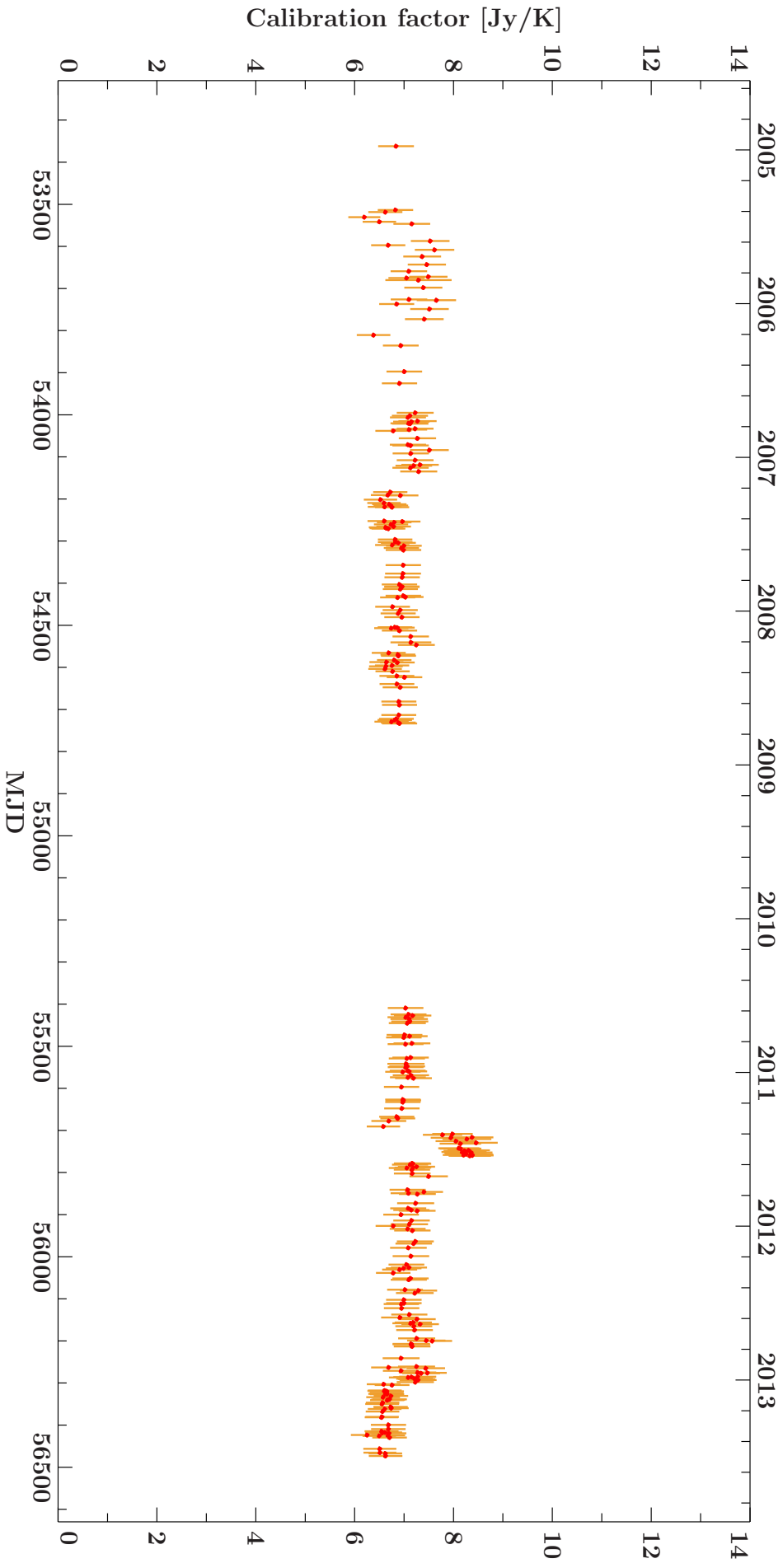


Figure 3.9.: The time evolution of the calibration factor S_{cal}/T_{cal} of the selected observations of 3C123. This source gives a similarly good coverage over the whole time range as Hyd A. The steps in the antenna gain are visible again.

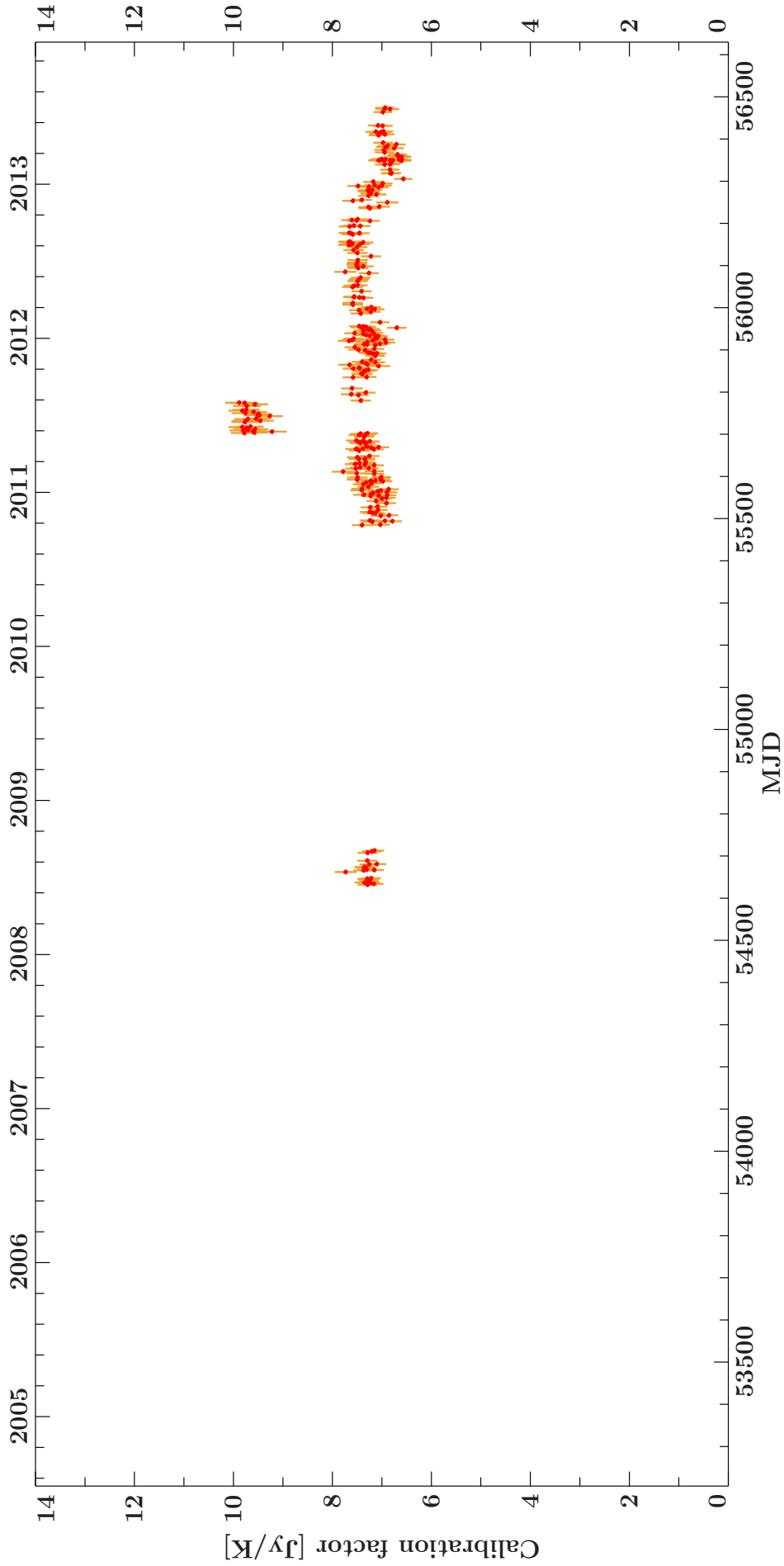


Figure 3.10.: The time evolution of the calibration factor S_{cal}/T_{cal} of the selected observations of J1939-6342. This source has no coverage at times before the spring of 2008.

3.4. The lightcurve of PKS 0637-752

With the calibration observations selected in the last section, the lightcurve of PKS 0637-752 has been extracted to demonstrate the capabilities and problems of the process.

Figure 3.11 shows the lightcurve of PKS 0637-752 at $f = 8280$ MHz, calibrated with the Hyd A observations as described before. It exhibits a strong step in the flux density in the time region of the secondary reflector positioning problems in 2011. A zoom into this time region of the lightcurve is depicted in Fig. 3.12 together with the corresponding detail of the calibration factor measurements. The feature in the lightcurve of PKS 0637-752 perfectly aligns with the problematic time range, leading to the assumption that the calibration is insufficient in this region.

Figure 3.13 and Fig. 3.14 show the same data of PKS 0637-752 as Fig. 3.11 but calibrated with the selected calibration observations of 3C123 and J1939-6342. The 2011 feature in the lightcurve calibrated with 3C123 is less prominent as before (see Fig. 3.15), with J1939-6342 as calibrator it disappears completely, as Fig. 3.16 shows. However, the different calibrator sources also result in slightly different average flux densities of PKS 0637-752.

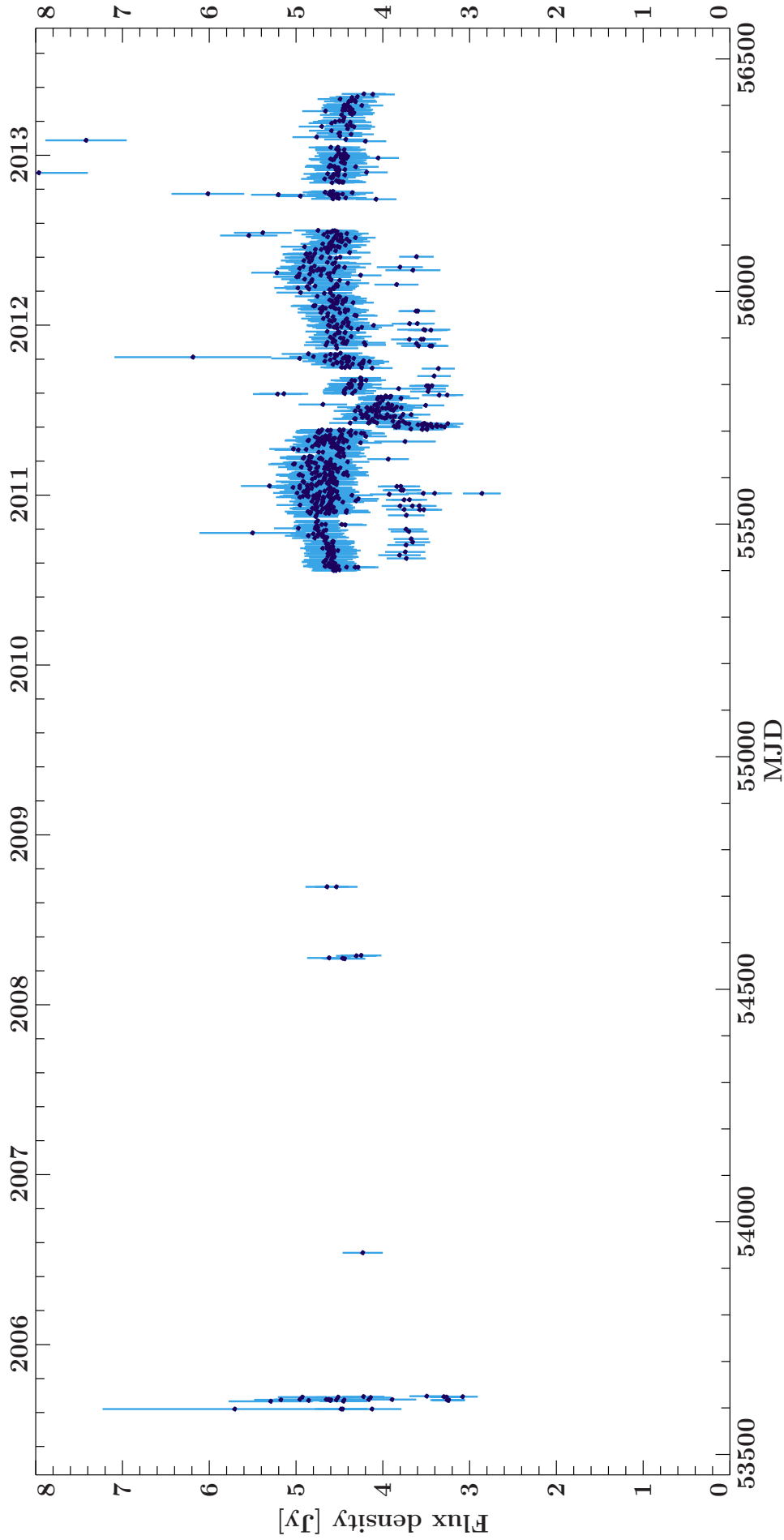


Figure 3.11.: The lightcurve of PKS 0637-752 at $f = 8280$ MHz. In this plot, all available data are presented. The calibration is described in the text. The low outliers at about the same level are thought to be caused by the dichroic reflector being installed for these observations, which is not tracked in the input files and must be examined in detail for each file using the observatory's logbook.

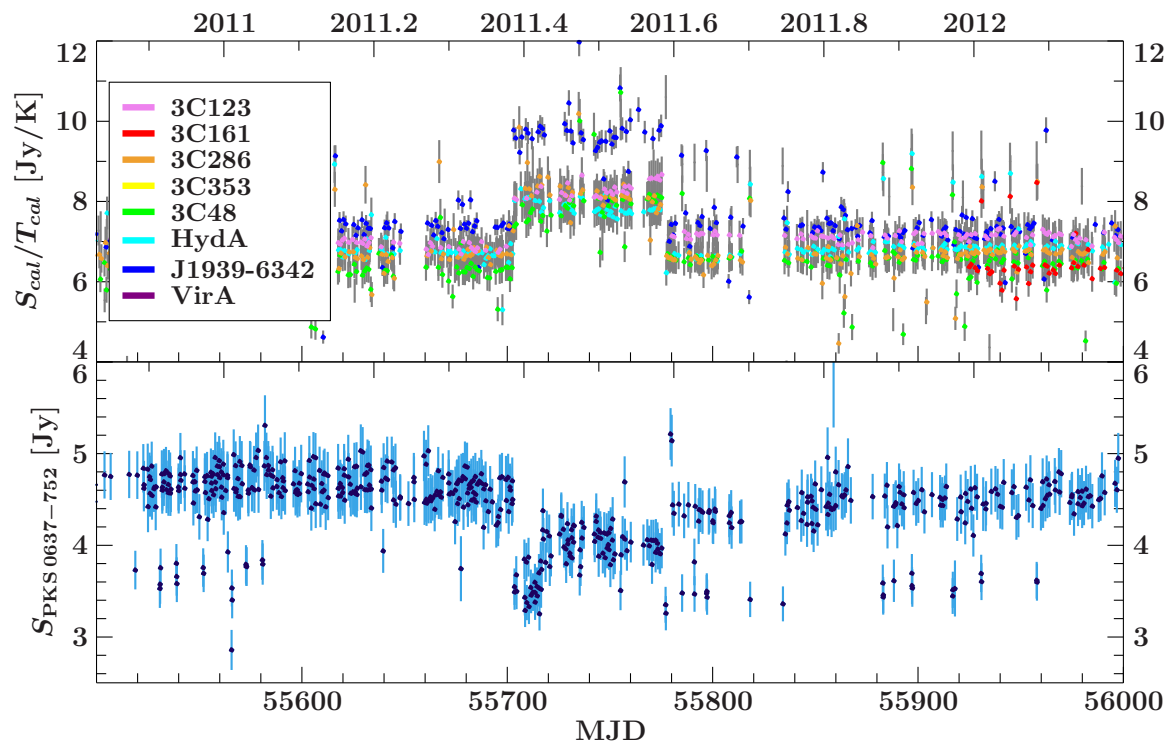


Figure 3.12.: The lightcurve of PKS 0637-752 around the time of the secondary reflector problems compared to the calibration factor. It can be seen that the “feature” in the lightcurve aligns exactly with the problematic time. This indicates that the feature is an artifact of the calibration.

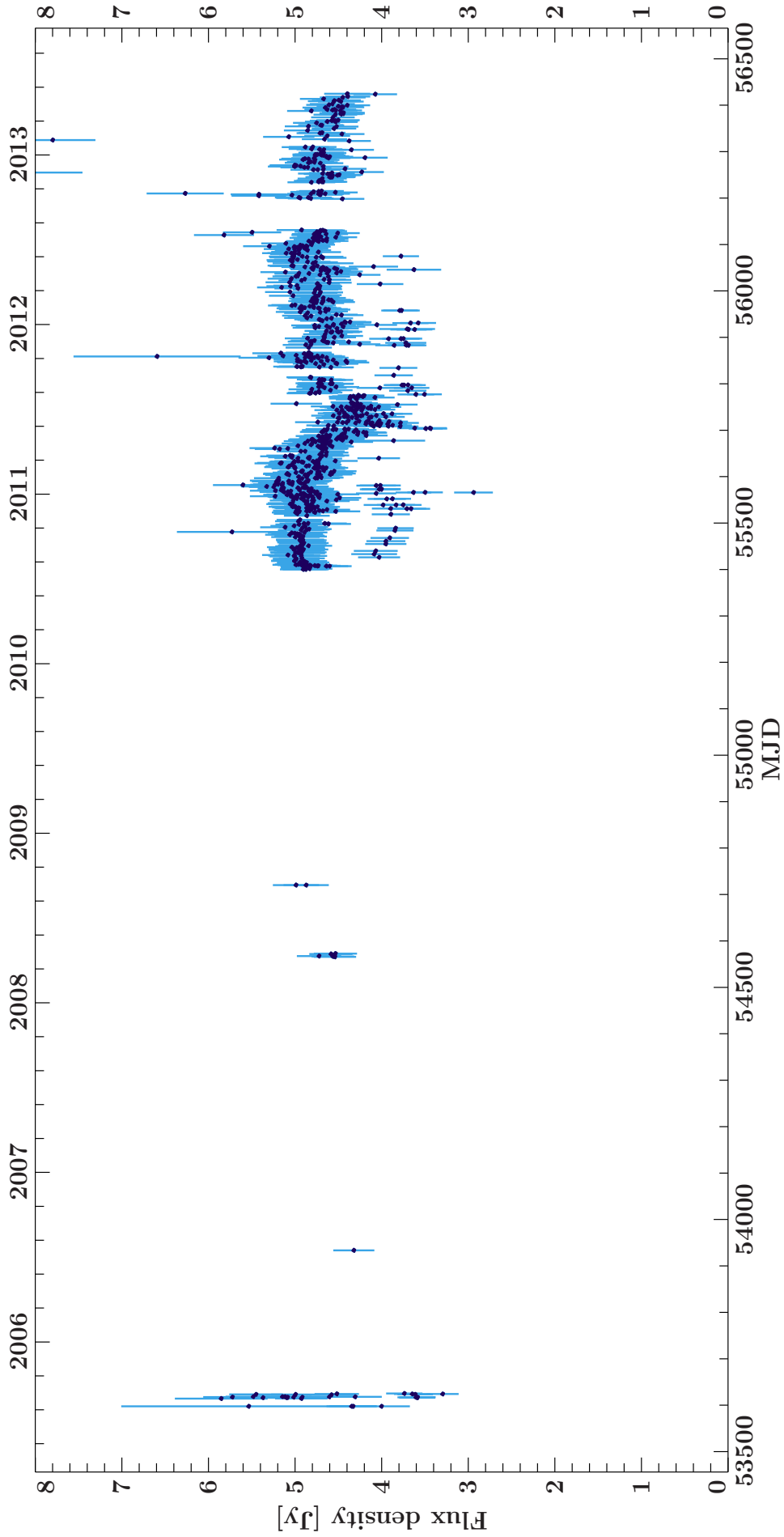


Figure 3.13.: The lightcurve of PKS 0637-752 as in Fig. 3.11, but this time calibrated with observations of 3C123.

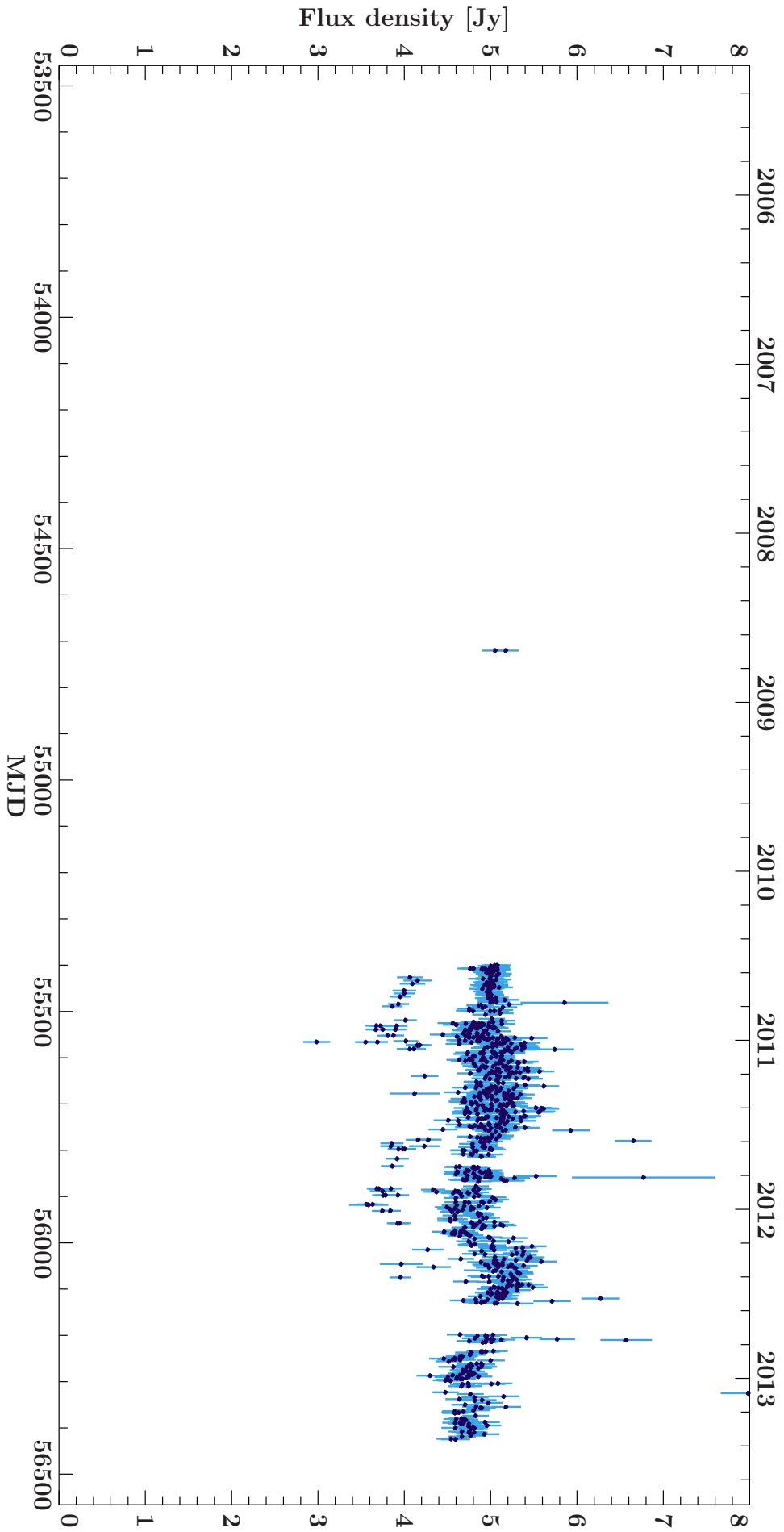


Figure 3.14.: The lightcurve of PKS 0637-752 as in Fig. 3.11 and fig. 3.13, but this time calibrated with observations of J1939-6342.

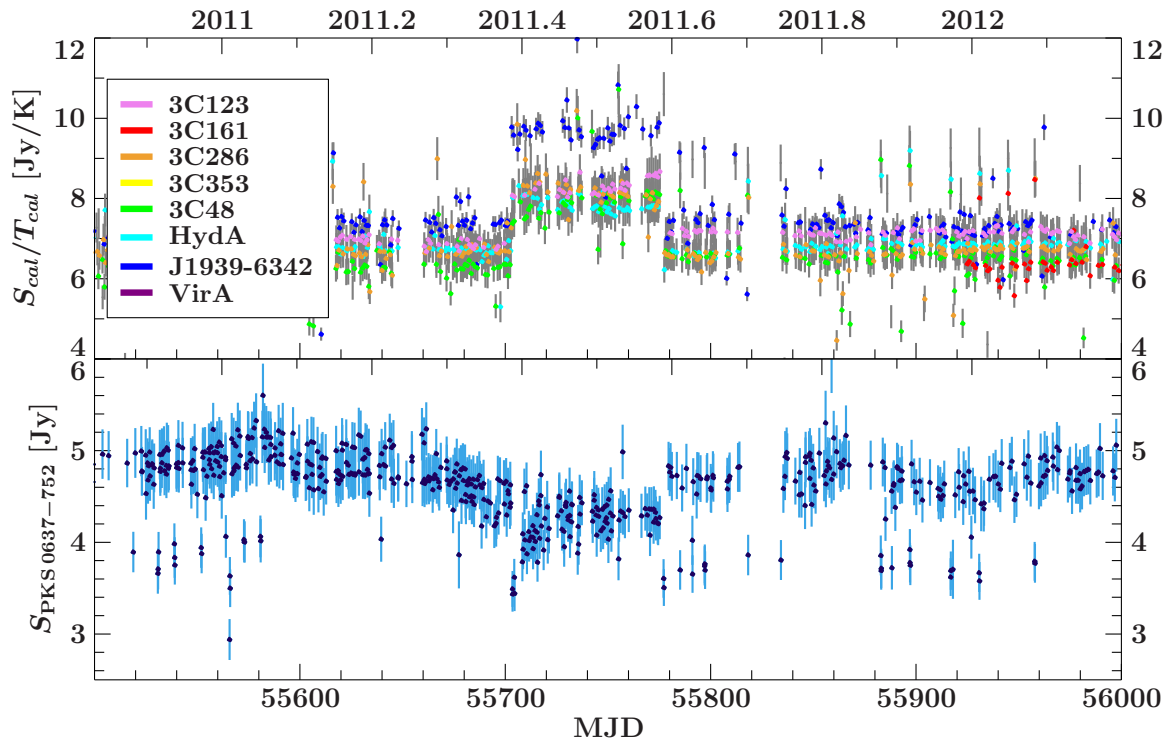


Figure 3.15.: The same plot as Fig. 3.12, but this time with the source 3C123 as calibrator. The feature changed its appearance visibly.

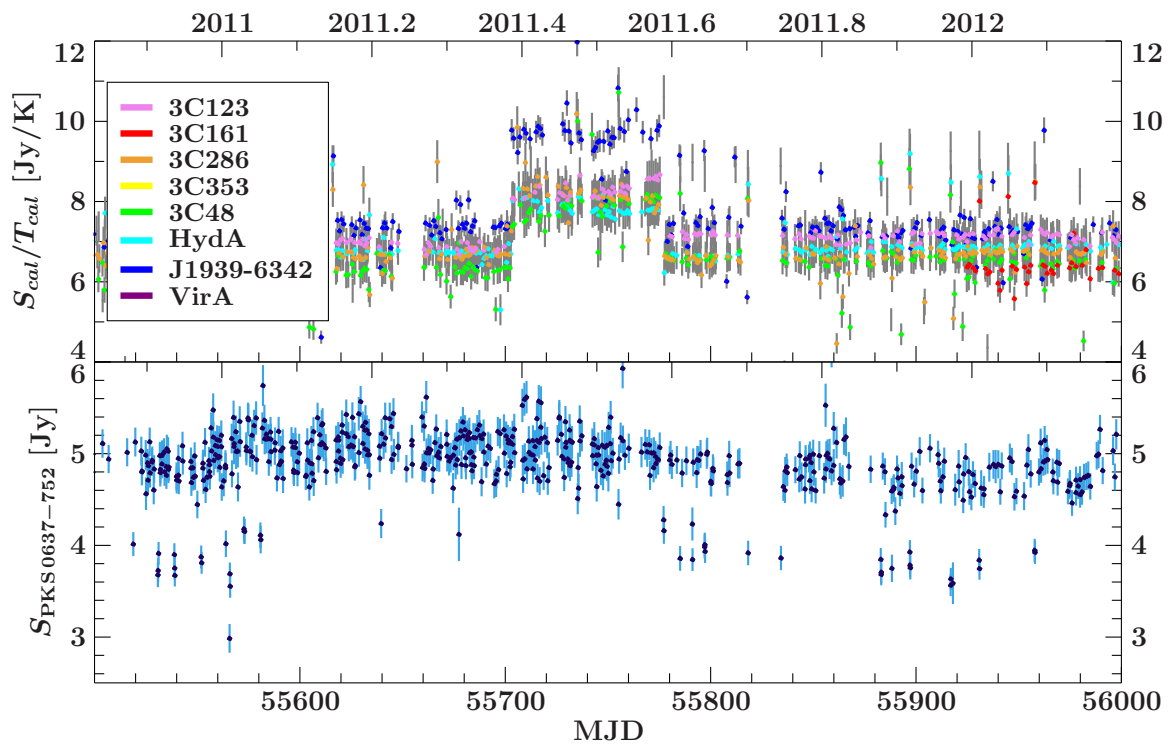


Figure 3.16.: The same plot as Fig. 3.12 and Fig. 3.15, but this time with the source J1939-6342 as calibrator. The feature almost disappears.

4. Conclusions and Outlook

This work has shown that it is possible to analyze huge data sets of the Hartebeesthoek 26 m radio telescope automatically. By fitting sections through the two-dimensional PSF simultaneously to all subscans of one observation it is possible to achieve good results even if individual subscans have bad data quality.

The only exception of the automation is the selection of calibration observations to be ingested into the CSDB. It is necessary to control the quality of the calibration data before it is used for further calculations because bad fits or faulty assumptions can cause strong fluctuations in output lightcurves. An example for the importance of exact calibration has been shown with the lightcurve of PKS 0637-752. The inaccurate secondary focus alignment in 2011 has caused a jump in the telescope's sensitivity which is not compensated by each of the three calibrator sources that have been used.

A further examination of the calibration data has revealed other features like the correlation between the angular distance of the observed source to the Sun and the value of the calibration factor. This dependency has to be investigated in the future to be able to correct for it.

It has also been shown that different calibrator sources tend to result in different calibration factors. It is assumed that this is due to their position on the sky which leads to gravitational deformations of the beam pattern. Such an effect has been predicted, but has not been measured in the course of this work. However, the fit program has been prepared to include a correction for this effect. Next steps to solve this problem are to measure the beam pattern at different pointing positions at high resolutions and to examine the differences between them.

When the gravitational deformation is measured, the assumption of point-sources has to be questioned. To wrongly assume that the signal part of the source is a section through the PSF itself can cause errors in the determination of the amplitude and thus the source flux density. Instead, the spatial structure of the source has to be taken into account by a convolution with the beam pattern.

With the programs described in this work, a tool has been developed which enables the investigation of these fine calibration problems without having to pay attention to the rather technical part of fitting and data handling. Instead, in short time and with very low effort, huge amounts of data can be processed automatically. The program is laid out such that new calibration data only requires to reprocess the steps which are changed by the fresh information. This enables experimenting with new calibration methods even for the whole data sample to maximize the statistical evidence of the idea. The outcome of this task will not only provide information about astronomical sources but also a better understanding of the instrument itself.

5. Abbreviations

<i>ADB</i>	Analysis Database
<i>AGN</i>	Active Galactic Nucleus
<i>CALDB</i>	Calibration Database
<i>CIF</i>	Calibration Index File
<i>CSDB</i>	Calibration Source Database
<i>FITS</i>	Flexible Image Transport System
<i>GMST</i>	Greenwich Mean Sidereal Time
<i>GSL</i>	Gnu Scientific Library
<i>HartRAO</i>	Hartebeesthoek Radio Astronomy Observatory
<i>LMST</i>	Local Mean Sidereal Time
<i>PIL</i>	Parameter Interface Library
<i>PSF</i>	Point Spread Function
<i>TANAMI</i>	Tracking Active Galactic Nuclei with Austral Milliarcsecond Interferometry
<i>UT1</i>	longitude corrected Universal Time
<i>VLA</i>	Very Large Array
<i>VLBI</i>	Very Long Baseline Interferometry

A. Appendix

A.1. CIF binary table definition

In the following, the columns of the CIF's binary table are listed.

- **TELESCOP** (20-character string):
The telescope's name.
- **INSTRUME** (10-character string):
The receiver frequency of the calibration file data (MHz).
- **DETNAM** (20-character string):
The PHASECAL-keyword of the calibration raw data.
- **FILTER** (10-character string):
The DICHOIC-keyword of the calibration raw data.
- **CAL_CLAS** (3-character string):
The class of the calibration file. Allowed values:
 - “USR”: A user-defined calibration file.
 - “PCF”: A primary calibration file.
 - “BCF”: A basic calibration file.
 - “CPF”: A calibration product file.

Note: The value of this key is not checked in the recent version.

- **CAL_DTYP** (4-character string):
A flag for simulated (“SIMU”) or measured (“MEAS”) data sets.
- **CAL_CNAM** (20-character string):
The calibration data type (“2D_PSF” or “OBSPAR”).
- **CAL_VSD** (10-character string):
The validity date when the calibration data can be first used in yyyy-mm-dd format.
- **CAL_VST** (8-character string):
The UTC time on the day CAL_VSD from which this calibration data can be used in hh:mm:ss format.
- **CAL_DEV** (20-character string):
The environment variable to the calibration data file location on the file system.
- **CAL_DIR** (127-character string):
The path to the calibration data file.
- **CAL_FILE** (255-character string):
The file name of the calibration data.

- **CAL_XNO** (integer):

The extension number of the calibration data.

The CALDB is located in

`$SDA_PATH/CALDB/` .

The CIF is the first binary table extension of the file

`$SDA_PATH/CALDB/HARTRAO.cif` .

The calibration files are stored in the directories

`$SDA_PATH/CALDB/2D_PSF/`

and

`$SDA_PATH/CALDB/OBSPAR/`.

The names of calibration files are constructed by using key values of their description in the following format:

`CNAM_CAL_VSD_CAL_VST_TELESCOP_INSTRUME_DETNAM_FILTER.fits`

A.2. CIF utility tools

Two tools are provided to add and remove calibration data from the CIF. These are described in the following.

A.2.1. Ingesting calibration files

To ingest a new calibration file, the program `add_calfile` may be used. It has the following parameters:

- **dev** (string type):
An environment variable to the input file.
- **path** (string type):
The path to the input file.
- **file** (string type):
The input file's name.
- **cal_clas** (string type):
The class of the calibration file (“USR”, “PCF”, “BCF”, “CPF”, same as above).
- **cal_dtyp** (string type):
The flag for simulated (“SIMU”) or measured (“MEAS”) data sets (same as above).
- **cal_cnam** (string type):
The type of calibration file (“2D_PSF” or “OBSPAR”, same as above).
- **cal_vsd** (string type):
The validity starting date in `yyyy-mm-dd` format (same as above).
- **cal_vst** (string type):
The validity starting time in `hh:mm:ss` format (same as above).

The last five parameters are directly the keys which will be written into the CIF. After launch of `add_calfile`, these parameters are read via the PIL, and in case not all are given in the command line, the user is prompted to enter them one by one.

Then the input file is opened and the remaining CIF-keys are obtained by reading the respective FITS-keywords.

The calibration file is ingested by copying it into the CALDB directory and adding the entry into the CIF. The original file is left unmodified.

A.2.2. Removing calibration files

To remove a file from the calibration database, the program `remove_calfiles` should be used. It has a single argument, read in via the PIL:

- `expression` (string type): An expression describing the files to be deleted from CALDB.

This argument is meant to be an expression following the rules of the FITS Extended Filename Syntax, and all files in the CIF matching to this expression are removed. Therefore, a temporary copy of the table is filtered for all matching entries, which are then deleted from the CALDB-directories. Afterwards, the rows in the original CIF matching to the expression are removed.

A.3. Beam fitting program

The procedure discussed in Sect. 2.5 is implemented in the program `beamfit`. Like most tools written for this work, it uses the PIL for input argument handling. As the function is very complex, it has a relatively large number of parameter options. These are listed in the following:

- `dev` (string):
The environment variable to the input data file location on the file system.
- `path` (string):
The path to the input data file location on the file system.
- `file` (string):
The name of the input data file.
- `manflagging` (integer):
If set to 1, the user is prompted to flag the analysis based on a plot.
- `plot_init_model` (integer):
If set to 1, the initial model is plotted before the fit.
- `plot_result` (integer):
If set to 1, the result is plotted (even if `manflagging` is 0).
- `save_path` (integer):
If set to 1, the model components and data point values are saved additionally in the extension `SCANDATA`.
- `calc_uncert` (integer):
If set to 1, the uncertainties of the model parameters are estimated by probing the χ^2 -landscape.

- **stem** (string):
An optional string which is appended to the standard output filename.
- **tmp** (integer):
If set to 1, the analysis will not be ingested directly by the program (see Sect. 2.8).
- **distortion_corr** (integer):
If set to 1, the distortion correction is turned on. If the function is not known and implemented, it can be set to 0 to save calculation time.
- **calc_chisq_cuts** (integer):
If set to 1, additional 1D-sections through the χ^2 -landscape are calculated and saved.
- **calc_chisq_landsc** (integer):
If set to 1, a 2D- χ^2 -landscape is calculated and saved as a FITS-image.
- **ls_par1** (integer):
If **calc_chisq_landsc** is set to 1, the parameter with this index will be stepped at the x-axis.
- **ls_par2** (integer):
If **calc_chisq_landsc**, the parameter with this index will be stepped at the y-axis.
- **fix_amp_factor** (integer):
If set to 1, the amplitude factor of the second beam (if turned on in the scan) will be frozen to -1 .
- **limit_datarange** (integer):
If set to 1, data points with a coordinate distance of more than the width of the main beam to both components will be ignored. The distance is measured after an initial fit to all data points. The program aborts if all data points of a subscan are ignored.
- **gausserrors** (integer):
If set to 1, the data point errors will be estimated by measuring the width of a Gaussian function fitted to the distribution of the differences between data points and the model evaluated at their coordinates after an initial fit.

All of these parameters are “hidden”. This means, that if no argument for them is given in the command line at program launch, the default value defined in the `beamfit.par`-file is used. This is particularly useful for parameters which are used with the same value in most cases.

An example program call could be:

```
./beamfit manflagging=0 calc_chisq_landsc=0 calc_chisq_cuts=0 calc_uncert=1
dev="RADIO" path="0637-752/" file="2013d132_16h05m26s_Cont_jon_0637-75.fits"
tmp=0 save_path=0
```

This call will analyze the data file

```
$RADIO/0637-752/2013d132_16h05m26s_Cont_jon_0637-75.fits
```

and estimate the uncertainties of the best-fit parameter values. It will not produce any additional files and the resulting analysis will be ingested immediately into the ADB.

A.4. Fit output file definition

The standard output file of the program `beamfit` has the following extensions:

- Primary
- Frontend extension
- FIT_PARS

The **Primary** extension contains all required information from the input file as well as its directory and file name. It also includes the keywords **DPROC** and **PROCBY** which give the system time of the analysis process and the name of the user logged in during that time.

The frontend extension is a copy of the one in the input file.

In the binary table extension **FIT_PARS**, the model parameters are saved. In its header, the following keywords are most important to the analysis:

- **SCANS**: The number of subscans (N_{subscans}) of the observation.
- **CENTFREQ**: The central value of the frequency band used for this observation ([MHz]).
- **BANDWIDTH**: The frequency bandwidth ([MHz]).

It also includes information about the quality of the fit (**RCHISQ**), the manual flag value (**MANFLAG**), the count rate-antenna temperature conversion factors for both polarization channels (**HZPERK1/2**) as well as eight parameters characterizing the residual distribution:

- **MED1/2**: The median of the residuals in both channels.
- **STDDEV1/2**: The standard deviation of the residuals in both channels.
- **SKEW1/2**: The skewness of the residuals in both channels.
- **KURT1/2**: The kurtosis of the residuals in both channels.

The parameter values and their uncertainties are saved in the binary table itself. This table has $1 + 6 + 2 \times N_{\text{subscans}}$ columns and 8 rows. The first 7 columns have the following names:

1. **NAME** (20-character string): A descriptor of the row
2. **RA** (double precision float):
Information about the *ra*-value of the source position in [deg].
3. **DEC** (double precision float):
Information about the *dec*-value of the source position in [deg].
4. **AMP** (double precision float):
Information about the amplitude of the source A_1 in the first beam component in [Hz].
5. **RA2** (double precision float):
Information about the *dx*-value of the second beam position offset in [deg].
6. **DEC2** (double precision float):
Information about the *dy*-value of the second beam position offset in [deg].
7. **AMP2** (double precision float):
Information about the amplitude factor A_2 of the second beam in [Hz].

While the columns 2-7 describe the source signal-part of the model, the remaining columns contain all information about the background model parameters. Alternately, the constant parameter of the background (**C**) and the linear one (**L**) are listed. The units are [Hz] and [Hz/deg], respectively.

The 8 rows contain not only the best-fit-values of the parameters, but also their uncertainties are included. The content of each row is described in the **NAME**-column:

1. **Ch1_abs**:

The absolute value of the parameter in polarization channel 1.

2. **Ch2_abs**:

The absolute value of the parameter in polarization channel 2.

3. **Ch1_err_mpf1s**:

The MPFIT-estimate for the 1σ -uncertainty of the parameter in polarization channel 1.

4. **Ch2_err_mpf1s**:

The MPFIT-estimate for the 1σ -uncertainty of the parameter in polarization channel 2.

5. **Ch1_err_dch21_l**:

The $(\Delta\chi^2 = 1)$ -probing estimate for the uncertainty of the parameter in polarization channel 1 (lower uncertainty).

6. **Ch2_err_dch21_l**:

The $(\Delta\chi^2 = 1)$ -probing estimate for the uncertainty of the parameter in polarization channel 2 (lower uncertainty).

7. **Ch1_err_dch21_u**:

The $(\Delta\chi^2 = 1)$ -probing estimate for the uncertainty of the parameter in polarization channel 1 (upper uncertainty).

8. **Ch2_err_dch21_u**:

The $(\Delta\chi^2 = 1)$ -probing estimate for the uncertainty of the parameter in polarization channel 2 (upper uncertainty).

The files containing the analysis results are saved in

`$SDA_PATH/analysis/YYYY/YYYY.MM/`

with `YYYY` being the year in which the data was recorded, and `MM` being the month. The filename is

`tMJD1000_JRAhhmmDEC10.fits`

with MJD_{1000} being $mjd \cdot 1000$, RA_{hhmm} being ra in the format `hhmm` and DEC_{10} being $dec \cdot 10$.

A.5. ADB binary table definition

The ADB is a FITS-binary table extension and has the following 29 columns:

- **TELESCOP** (20-character string):

The telescope's name.

- **RAJ2000** (double precision float):
The reference source position in *ra* (J2000 system).
- **DECJ2000** (double precision float):
The reference source position in *dec* (J2000 system).
- **TIME** (20-character string):
The time mark of the original data file.
- **MJD** (double precision float):
The start time of the scan.
- **PROCDATE** (20-character string):
The system time when the analysis was made.
- **FREQ** (double precision float):
The central receiver frequency of the observation.
- **UNCERT** (integer):
A flag for the uncertainty estimation.
- **FLUXCAL** (integer):
A flag for flux calibration.
- **FLAG** (integer):
A flag for other criteria (manual flagging, external filters).
- **ODATA** (255-character string):
The name of the original data file.
- **DICKE** (20-character string):
The “DICKE” status.
- **DICHROIC** (10-character string):
The status of the “DICHROIC”-Keyword.
- **PHASECAL** (10-character string):
The status of the “PHASECAL”-Keyword.
- **DEV** (20-character string):
The environment variable to the analysis file location on the file system.
- **PATH** (127-character string):
The path to the analysis file.
- **FILE** (255-character string):
The name of the analysis file.
- **OBSERVER** (20-character string):
The name of the observer.
- **PROPOSAL** (20-character string):
The proposal id.

- **DIODECAL** (integer):
A flag for diode calibration information.
- **REDCHISQ** (double precision float):
The reduced χ^2 of the fit.
- **A1AV** (double precision float):
The average of the main amplitudes in both polarization channels [Hz].
- **A2FCTAV** (double precision float):
The average of the second beam amplitude factors in both polarization channels.
- **MEDAV** (double precision float):
The average of the median residual values in both polarization channels.
- **STDEVAV** (double precision float):
The average of the residuals' standard deviation values in both polarization channels.
- **ACH1** (double precision float):
The fitted source amplitude in channel 1 [Hz].
- **ACH2** (double precision float):
The fitted source amplitude in channel 2 [Hz].
- **CCH1** (double precision float):
The [Hz/K]-conversion factor for channel 1.
- **CCH2** (double precision float):
The [Hz/K]-conversion factor for channel 2.

The file is located in

`$SDA_PATH/analysis/` .

The ADB is the first binary table extension of the file

`$SDA_PATH/analysis/HARTRAO.adb` .

A.6. Filtering ADB files

An ADB-file can be filtered by using the tool `adbfilter`. The syntax is:

```
./adbfilter [input file] [expression] [output file]
```

Here `expression` is a filtering expression following the FITS Extended Filename Syntax rules. The `output file` is an ADB-conform FITS file which includes all rows of `input file` matching this expression. For safety reasons, the file names have to be different from each other, such that the original ADB file can not be overwritten by accident.

If one or more files have to be removed from the ADB, the tool `adbfilter` should be used as well. Therefore the filter expression has to be formulated such that the files to be removed will be filtered out. The resulting file can be swapped with the original ADB file afterwards. Note that this process will not affect the analysis data file itself. It has to be deleted manually if desired.

There are two possibilities to ingest an analysis into the ADB. The standard option is to automatically record the new analysis file directly in the `beamfit` program. If the parameter `tmp` is set to 0, the new file is ingested after its creation.

However, if this is undesired, `tmp` can be set to 1. Then, a temporary file with the analysis file's path and name is created in

`$SDA_PATH/analysis/TMP/` .

This option should be used if the program is executed multiple times in parallel on computing clusters. Otherwise, the ADB file would be manipulated from several clones of `beamfit` at the same time, leading to read- and write-errors. Instead, after all jobs are completed and all temporary files are created, the tool `adb_ingestor` should be used. This program collects all temporary files created from `beamfit` in the path specified by the parameter `tpath` and ingests the respective analysis files in sequence. The temporary files are not deleted by this program itself, this must be done manually after checking its success.

A.7. CSDB binary table definition

The CSDB is a FITS-binary table extension. The table has the following 20 columns:

- **TELESCOP** (20-character string):
The telescope's name.
- **RAJ2000** (double precision float):
The reference source position in *ra* (J2000 system).
- **DECJ2000** (double precision float):
The reference source position in *dec* (J2000 system).
- **TIME** (20-character string):
The time mark of the original data file.
- **MJD** (double precision float):
The start time of the scan.
- **PROCDATE** (20-character string):
The system time when the analysis was made.
- **FREQ** (double precision float):
The central receiver frequency of the observation.
- **BANDWIDTH** (double precision float):
The frequency bandwidth of the observation.
- **ODATA** (255-character string):
The name of the original data file.
- **DICKE** (20-character string):
The "DICKE" status.
- **DICHROIC** (10-character string):
The status of the "DICHROIC"-Keyword.

- **PHASECAL** (10-character string):
The status of the “PHASECAL”-Keyword.
- **DEV** (20-character string):
The environment variable to the analysis file location on the file system.
- **PATH** (127-character string):
The path to the analysis file.
- **FILE** (255-character string):
The name of the analysis file.
- **OBSERVER** (20-character string):
The name of the observer.
- **PROPOSAL** (20-character string):
The proposal id.
- **REDCHISQ** (double precision float):
The reduced χ^2 of the fit.
- **CONVFAC** (double precision float):
The reduced χ^2 of the fit.
- **DCONVFAC** (double precision float):
The reduced χ^2 of the fit.

The CSDB is located in

`$SDA_PATH/CALDB/` .

It is the first binary table extension of the file

`$SDA_PATH/CALDB/HARTRAO.csdb` .

A.8. Ingesting calibration source observations

To examine and ingest a large number of calibration source observations which are listed in an ADB file, the tool `csdb_ingestor` can be used. It has 6 PIL-parameters:

- **dev**: The environment variable to an ADB-conform file on the file system.
- **path**: The path to an ADB-conform file on the file system.
- **file**: The name of an ADB-conform file with the input calibration observations.
- **freq**: The frequency for which calibrator sources shall be examined.
- **optfilter**: If set to 1, the optional filter `filter` will be used.
- **filter**: An optional filter in the FITS-Extended Filename Syntax.

After program launch, the analysis files with matching frequency in the input ADB file which describe a source known to the internal calibrator list for this frequency are loaded and checked.

All files which are possible calibration files are plotted, as illustrated in Fig. A.1. Also, histograms of the distributions of χ_{red}^2 , S_{cal}/T_{cal} and $\Delta(S_{cal}/T_{cal})$ are shown.

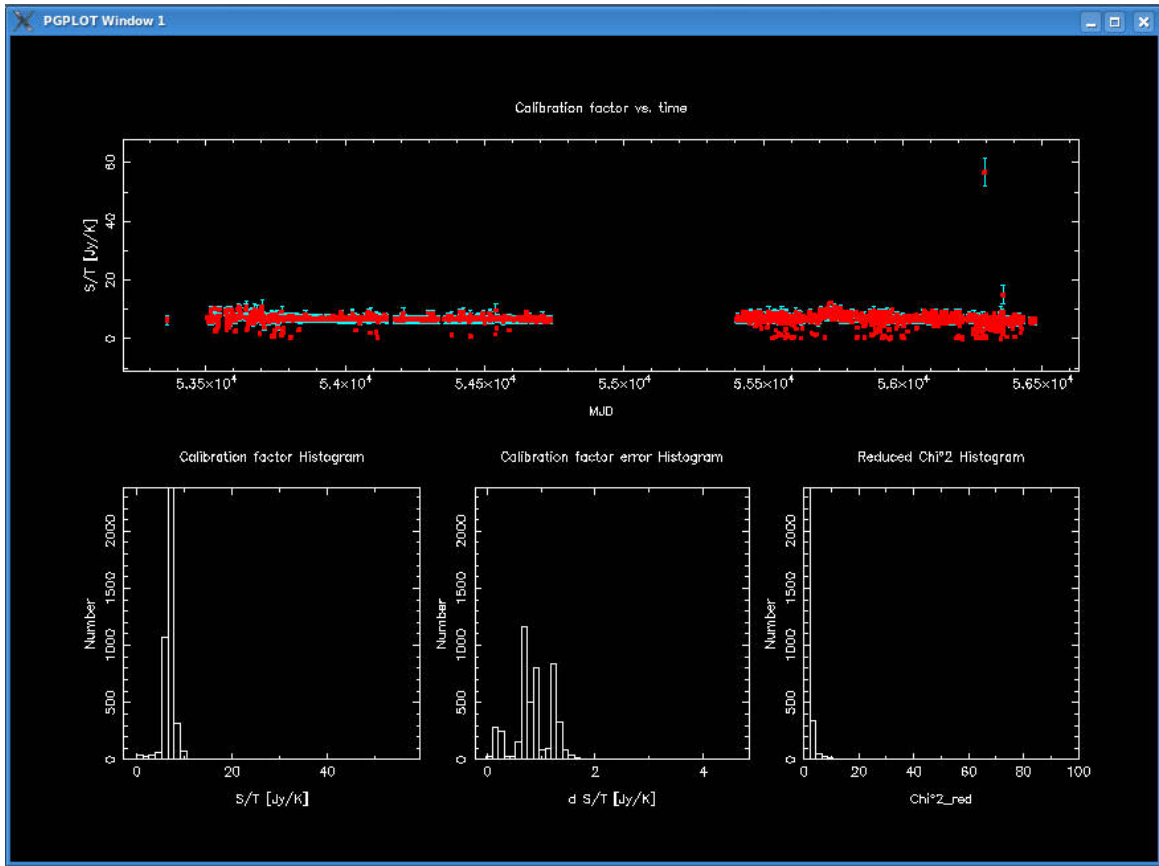


Figure A.1.: A screenshot of the plot panel of the `csdb_ingestor-tool`. On the top, the time evolution of the calibration factor is shown. Below are histograms of the distributions of S_{cal}/T_{cal} , $\Delta(S_{cal}/T_{cal})$ and χ^2_{red} . With the help of these plots, the calibration observations to be ingested can be selected.

On the command line, commands can be given interactively to set criteria for data points. Analyses which do not fit these cuts are deleted from the plots. With the `restore` -command, the last manipulation can be reversed.

When all remaining data points are meant to be ingested, the `save`-command can be entered. Then, the entries are added to the CSDB and the respective analysis files are copied into the directory

```
$SDA_PATH/CALDB/CALSRC/ .
```

The ADB and the original analysis files remain unchanged. From now on, the ingested observations can be used for flux calibration.

A.9. Calibrating source flux densities

A tool which calibrates source observations which are listed in the ADB is provided. It is called `calibrate_flux_adb` and has two input arguments: `optfilter` and `filter`.

If `optfilter` is set to 1, the string given by `filter` is used as a FITS Extended Filename Syntax expression for the ADB. All observations that match this expression are then flux calibrated. If `optfilter` is 0, all observations in the ADB are calibrated.

A.10. Flux calibration output definition

The calibrated flux is saved in the **FLUXCAL** extension of the analysis file. It contains three columns:

- **FLUXDENS** (double precision float):

The calibrated flux density in [Jy].

- **DFLUXDENS** (double precision float):

The uncertainty of the flux density in [Jy].

- **CALSRCFILE** (255-character string):

The filename of the calibration source observation used for this calibration.

After an observation is calibrated successfully, the value of **FLUXCAL** in the **FIT_PARS** extension of the analysis file and in the ADB-entry for this file is set to 1.

Bibliography

- author unknown 2010, Monthly Notes of the Astronomical Society of South Africa 69, 168
- Baars J.W.M., Genzel R., Pauliny-Toth I.I.K., Witzel A., 1977, A&A61, 99
- Borkowski J., Lock T., Walter R., 2002, Parameter Interface Library Users Manual
- Crawford A., Hogg D., Hunt L., et al., 1961
- Gaylard M., 2012, Radio Astronomy with a Single-Dish Radio Telescope
- Gaylard M., Buchner S., 2003, HartRAO Keywords, priv. com.
- George I.M., Breedon L., Corcoran M.F., 1998, HEASARC Calibration Memo CAL/GEN/92-011
- Gordon W., Lalonde L., 1961, IEEE Transactions on Antennas and Propagation 9, 17
- Hachenberg O., Grahl B.H., Wielebinski R., 1973, IEEE Proceedings 61, 1288
- Kardashev N.S., Kovalev Y.Y., Kellermann K.I., 2012, The Radio Science Bulletin No 343, p. 22-29 343, 22
- Kellermann K.I., Moran J.M., 2001, Annual Review of Astronomy and Astrophysics 39, 457
- Korolkov D.V., Pariiskii I.N., 1979, S&T57, 324
- Lampton M., Margon B., Bowyer S., 1976, ApJ208, 177
- Markwardt C.B., 2009, In: Bohlender D.A., Durand D., Dowler P. (eds.) Astronomical Data Analysis Software and Systems XVIII, Vol. 411. Astronomical Society of the Pacific Conference Series, p. 251
- Meeus J., 1998, Astronomical algorithms, Willmann-Bell
- Mink D.J., 1997, In: Hunt G., Payne H. (eds.) Astronomical Data Analysis Software and Systems VI, Vol. 125. Astronomical Society of the Pacific Conference Series, p. 249
- Müller C., Kadler M., Ojha R., et al., 2010, X-ray Astronomy 2009; Present Status, Multi-Wavelength Approach and Future Perspectives 1248, 481
- Pearson T., 2011, PGPLOT: Device-independent Graphics Package for Simple Scientific Graphs, Astrophysics Source Code Library
- Pence W., 1999, In: Mehringer D.M., Plante R.L., Roberts D.A. (eds.) Astronomical Data Analysis Software and Systems VIII, Vol. 172. Astronomical Society of the Pacific Conference Series, p. 487
- Pence W.D., 2010, CFITSIO: A FITS File Subroutine Library, Astrophysics Source Code Library
- Penzias A.A., Wilson R.W., 1965, ApJ142, 419
- Perley R.A., Chandler C.J., Butler B.J., Wrobel J.M., 2011, ApJL739, L1
- Reynolds J., 1994, ATNF Technical Memos 39.3/040, 1
- Rohlfs K., Wilson T., 2000, Tools of Radio Astronomy, Astronomy and Astrophysics Library, Springer-Verlag GmbH
- Ryle M., Vonberg D.D., 1948, Royal Society of London Proceedings Series A 193, 98
- Seidelmann P., Office U.S.N.O.N.A., Office G.B.N.A., 1992, Explanatory supplement to the Astronomical almanac, University Science Books
- Stanier H.M., 1950, Nature165, 354
- Thompson A.R., Clark B.G., Wade C.M., Napier P.J., 1980, ApJS44, 151
- Verschuur G., 2007, The Invisible Universe, Springer-Verlag
- Verschuur G., Kellermann K., Bouton E., 1988, Galactic and extragalactic radio astronomy, Astronomy and astrophysics library, Springer-Verlag
- Wells D.C., Greisen E.W., Harten R.H., 1981, A&AS44, 363

Acknowledgements

I would like to thank all people who helped me during the last months working on this thesis. My gratitude especially belongs to

- my supervisor Prof. Dr. Jörn Wilms (ECAP) for giving me the chance to work on this topic, his motivating words whenever they were needed, and to answer my questions whenever they appeared.
- Dr. Jonathan Quick (HartRAO) for helping me with the data analysis and providing me the observatory specific information.
- Dr. Roopesh Ojha (NASA GSFC/ORAU) for discussions about the development of the software.
- Christoph Grossberger (ECAP) for helping me with programming and plotting issues, for weekly discussions about the progress of the software development and data analysis, for useful comments after my test talk and for taking me to the observatory each week.
- Tobias Beuchert (ECAP) for introducing me to the basics of single-dish analysis and for providing me with the first ISIS-plotting scripts.
- Dr. Christian Schmid and Maria Hirsch (both ECAP) for the indispensable comments on the thesis and the test talk and for supporting me morally.
- Janina Lange for never getting tired of correcting my English, listening to the never ending stories of the problems during this thesis and for giving me counterbalance during the last year.

Furthermore, I'd like to thank the whole staff of the Dr. Karl Remeis-Sternwarte for the homely and friendly atmosphere.

Erklärung

Hiermit bestätige ich, dass ich diese Arbeit selbstständig und nur unter Verwendung der angegebenen Hilfsmittel angefertigt habe.

Erlangen,

Thorsten Brand